The Astrophysical Journal, 859:92 (23pp), 2018 June 1 https://doi.org/10.3847/1538-4357/aac01e

Extended Structures of Planetary Nebulae Detected in H_2 Emission*

Xuan Fang[1,2,8], Yong Zhang[1,3,4], Sun Kwok[1,2,9], Chih-Hao Hsia[5], Wayne Chau[4], Gerardo Ramos-Larios[6], and Martín A. Guerrero[7]

[1] Laboratory for Space Research, Faculty of Science, The University of Hong Kong, Hong Kong, People's Republic of China; fangx@hku.hk, zhangyong5@mail.sysu.edu.cn, sunkwok@hku.hk
[2] Department of Earth Sciences, Faculty of Science, The University of Hong Kong, Pokfulam Road, Hong Kong, People's Republic of China
[3] School of Physics and Astronomy, Sun Yat-Sen University, Zhuhai 519082, People's Republic of China
[4] Department of Physics, Faculty of Science, The University of Hong Kong, Pokfulam Road, Hong Kong, People's Republic of China
[5] Space Science Institute, Macau University of Science and Technology, Avenida Wai Long, Taipa, Macau, People's Republic of China
[6] Instituto de Astronomía y Meteorología, Av. Vallarta No. 2602, Col. Arcos Vallarta, CP 44130, Guadalajara, Jalisco, Mexico
[7] Instituto de Astrofísica de Andalucía (IAA, CSIC), Glorieta de la Astronomía s/n, E-18008 Granada, Spain
Received 2018 February 26; revised 2018 April 22; accepted 2018 April 23; published 2018 May 29

Abstract

We present narrowband near-infrared images of a sample of 11 Galactic planetary nebulae (PNe) obtained in the H_2 2.122 μm and Brγ 2.166 μm emission lines and the K_c 2.218 μm continuum. These images were collected with the Wide-field Infrared Camera on the 3.6 m Canada–France–Hawaii Telescope (CFHT); their unprecedented depth and wide field of view allow us to find extended nebular structures in H_2 emission in several PNe, some of these being the first detection. The nebular morphologies in H_2 emission are studied in analogy with the optical images, and indication of stellar wind interactions is discussed. In particular, the complete structure of the highly asymmetric halo in NGC 6772 is witnessed in H_2, which strongly suggests interaction with the interstellar medium. Our sample confirms the general correlation between H_2 emission and the bipolarity of PNe. The knotty or filamentary fine structures of the H_2 gas are resolved in the inner regions of several ring-like PNe, also confirming the previous argument that H_2 emission mostly comes from knots or clumps embedded within fully ionized material at the equatorial regions. Moreover, the H_2 image of the butterfly-shaped Sh 1-89, after removal of field stars, clearly reveals a tilted ring structure at the waist. These high-quality CFHT images justify follow-up detailed morphokinematic studies that are desired in order to deduce the true physical structures of a few PNe in the sample.

Key words: infrared: ISM – planetary nebulae: general – stars: AGB and post-AGB – stars: winds, outflows

1. Introduction

As descendants of the low- and intermediate-mass ($<$8–10 $M_\odot$) stars and the evolutionary stage right after the asymptotic giant branch (AGB), planetary nebulae (PNe) provide a fundamental tool to understand the interaction between stellar-synthesized materials and the interstellar medium (ISM). However, the mass-loss process of PNe remains a long-standing enigma. The modern view is that PNe are formed through interacting stellar winds (ISW; Kwok 1983) rather than a sudden ejection of the envelope of the progenitor AGB stars (Kwok et al. 1978; Kwok 1982). The mass-loss history may be dependent on the time and direction. Although the ISW model provides a general theoretical framework for understanding the shaping of PNe, the formation mechanism of detailed nebular structures revealed by sensitive observations, such as multipolar and point-symmetric structures (e.g., Balick 1987; López et al. 1998), is still poorly known.

The ISW model predicts the presence of AGB halos, which are often found around PNe (e.g., Balick et al. 1992). Different from the main nebulae that often appear to be highly asymmetric, the halos uniformly display spherical morphology, unless there are interactions between the PN halos and the ISM. Fast collimated outflows have been thought to be the primary agent for shaping the aspheric PNe (Sahai & Trauger 1998). The aspherical morphologies, with a majority characterized as bipolar or multipolar, are probably developed during the short transition from the early post-AGB to the PN phase, called the proto-PN phase (e.g., Sahai et al. 2011). However, why and when the stellar winds deviate from spherical symmetry are still in debate, although hydrodynamic simulations have been attempted to reproduce various axisymmetric shapes (e.g., Balick & Frank 2002).

Since the extended halos surrounding the main nebula often contain more mass than the optically bright PNe, detailed mappings of the optical nebular shell and the PN halo are essential for understanding the mass-loss history and dynamical evolutionary process of PNe. Because of their distances from the central star and the extinction due to dust, AGB halos are very faint in visible light (with typical surface brightness about 10^{-3} of the main PN shells). Optical observations have shown that the detected nebular masses are significantly lower than theoretical predictions; this is the

* Based on observations obtained with WIRCam, a joint project of CFHT, Taiwan, Korea, Canada, and France, at the Canada–France–Hawaii Telescope (CFHT), which is operated by the National Research Council (NRC) of Canada, the Institut National des Sciences de l'Univers of the Centre National de la Recherche Scientifique of France, and the University of Hawaii.
[8] Visiting Astronomer, Key Laboratory of Optical Astronomy, National Astronomical Observatories, Chinese Academy of Sciences (NAOC), 20A Datun Road, Chaoyang District, Beijing 100101, China.
[9] Visiting Professor, Department of Physics and Astronomy, University of British Columbia, Vancouver, B.C., Canada.

so-called "missing mass problem" in PNe (e.g., Kimura et al. 2012). Searching for extended structures around the main nebulae of PNe provides essential clues to solve this problem. Wide-field infrared (IR) imaging, which mainly traces the dust and molecular hydrogen (H_2) emission, therefore provides a powerful tool to study these extended structures. A case study was presented by Zhang et al. (2012b), who discovered a very extended ($\sim$40′ in diameter) halo around the Helix Nebula (NGC 7293) in the mid-IR emission; this bow-shaped halo signifies an interaction between the stellar wind and the ISM and suggests a complicated history of stellar mass loss.

The 2.122 μm 1-0 S(1) rovibrational emission line of H_2 is usually bright in warm, dense molecular regions and has been commonly used as a tracer of molecular gas in a variety of astrophysical environments, including PNe. This H_2 emission line has been detected in a number of Galactic PNe (e.g., Kastner et al. 1994, 1996; Latter et al. 1995; Schild 1995; Shupe et al. 1995; Guerrero et al. 2000; Arias et al. 2001; Ramos-Larios et al. 2008, 2012, 2017; Marquez-Lugo et al. 2013, 2015) as well as proto-PNe (e.g., Sahai et al. 1998; Hrivnak et al. 2008; Forde & Gledhill 2012). Imaging studies of the H_2 images of PNe have revealed that the H_2 2.122 μm emission in PNe is generally associated with a bipolar morphology (e.g., Webster et al. 1988; Zuckerman & Gatley 1988); this is known as *Gatley's rule*, and the possible astrophysics for this association is still discussed today (e.g., Ramos-Larios et al. 2017). The UKIRT Wide Field Infrared Survey for H_2 (UWISH2[10]; Froebrich et al. 2011) has detected H_2 emission from $\sim$280 candidate PNe and proto-PNe in the northern Galactic plane (Froebrich et al. 2015; Gledhill & Froebrich 2017), the majority of which were new detections, thus providing a rich database for the study of H_2 emission and PN morphologies.

H_2 emission can be excited by fluorescence or radiative pumping by the ultraviolet (UV) radiation from PN central stars (e.g., Black & van Dishoeck 1987; Dinerstein et al. 1988) or by shocked gas (e.g., Shull & Beckwith 1982; Burton et al. 1992). If the shocks are the dominant excitation mechanism, H_2 line emission can provide significant probes of the zones of dynamical interaction. For example, the multiple layers of halo in NGC 6720 have been observed in the H_2 2.122 μm emission, which might be shock excited (e.g., Kastner et al. 1994). Moreover, the H_2-to-Brγ emission line ratio has been found to correlate with the detailed morphologies of bipolar PNe (Guerrero et al. 2000; Ramos-Larios et al. 2017), which might be related to the dominant excitation mechanism of H_2. The relative strengths of H_2 emission lines with different excitation energies can also be used to trace the evolutionary status of PNe (Davis et al. 2003).

In order to search for extended nebular structures, we obtained deep near-IR images of a sample of Galactic PNe (see Figure 1) using the H_2, Brγ, and K_c narrowband filters on the Canada–France–Hawaii Telescope (CFHT). We introduce observations and data reduction in Section 2, and we describe morphologies in both the near-IR and optical emission lines in Section 3. We present extensive discussion in Section 4 and summarize our discussion in Section 5.

[10] http://astro.kent.ac.uk/uwish2

2. Observations and Data Reduction

2.1. CFHT Near-IR Observations

The deep near-IR imagery of a dozen Galactic PNe was carried out using the Wide-field InfraRed Camera (WIRCam; Puget et al. 2004) on the 3.6 m CFHT in 2012 August (program ID 12AS98). The wide-field imager WIRCam is composed of four HAWAII2-RG detectors (each 2048 × 2048 pixels) and covers a total field of view (FoV) of 20′ × 20′ with a pixel scale of 0.″3. The background emission from the sky and the telescope were removed by chopping and nodding during the observations. The nebular images were obtained in three narrowband filters: H_2 ($\lambda_c = 2.122\,\mu$m, $\Delta\lambda = 0.032\,\mu$m), Br$\gamma$ ($\lambda_c = 2.166\,\mu$m, $\Delta\lambda = 0.030\,\mu$m), and K_c ($\lambda_c = 2.218\,\mu$m, $\Delta\lambda = 0.033\,\mu$m). For each PN, at least 10 $\sim$60 s exposures were obtained with each of the three filters.

Observing nights were photometric; during the whole observing run, the seeing varied between 0.″5 and 0.″7. The average FWHM of the point sources in the H_2, Brγ, and K_c filters were 0.″55, 0.″51, and 0.″56, respectively. Images with the best quality were selected and reduced following standard procedure using IRAF[11] packages, including dark subtraction, flat-field correction, basic crosstalk removal, and sky subtraction using neighboring images. Separate exposure frames with sky subtraction were combined and mosaicked to produce the final images. A summary of the CFHT observations is given in Table 1. Flux calibration was not performed for our targets because no photometric standard stars were observed.

2.2. Narrowband Optical Imagery

Optical narrowband images of the PNe NGC 6445 and NGC 6781 were obtained with the Andalucía Faint Object Spectrograph and Camera (ALFOSC) on the 2.5 m Nordic Optical Telescope (NOT) at the Observatorio del Roque de los Muchachos (ORM, La Palma, Spain) in 2009 June. The optical images of NGC 6772, NGC 7048, and Sh 1-89 were obtained at the 1.5 m telescope at San Pedro Mártir (SPM) of the National Astronomical Observatory (OAN-SPM, Mexico) in 2009 August and 2010 June. For NGC 6445, NGC 6772, NGC 6781, and NGC 7048, narrowband filters centered at the [O III] λ5007, [N II] λ6583, and Hα emission lines were used in the observations; for Sh 1-89, the [N II] and Hα filters were used. The images obtained with the 2k × 2k CCD at the NOT have a plate scale of $\sim$0.″184 pixel^{-1}, while the 501 × 501 binned CCD at the 1.5 m SPM has a plate scale of 0.″504 pixel^{-1}. These optical images were first registered to the same orientation and sky coordinates (in J2000.0) and then rebinned to the same pixel scales as our CFHT images. This will allow a comparison study of nebular morphologies in the optical and IR bands. The color-composite images are presented in Figure 1.

2.3. The HST Archive Data

Archival *Hubble Space Telescope* (*HST*) optical and near-IR narrowband images were also used in our morphological study. These images were retrieved from the Mikulski Archive for

[11] IRAF, the Image Reduction and Analysis Facility, is distributed by the National Optical Astronomy Observatory, which is operated by the Association of Universities for Research in Astronomy under cooperative agreement with the National Science Foundation.

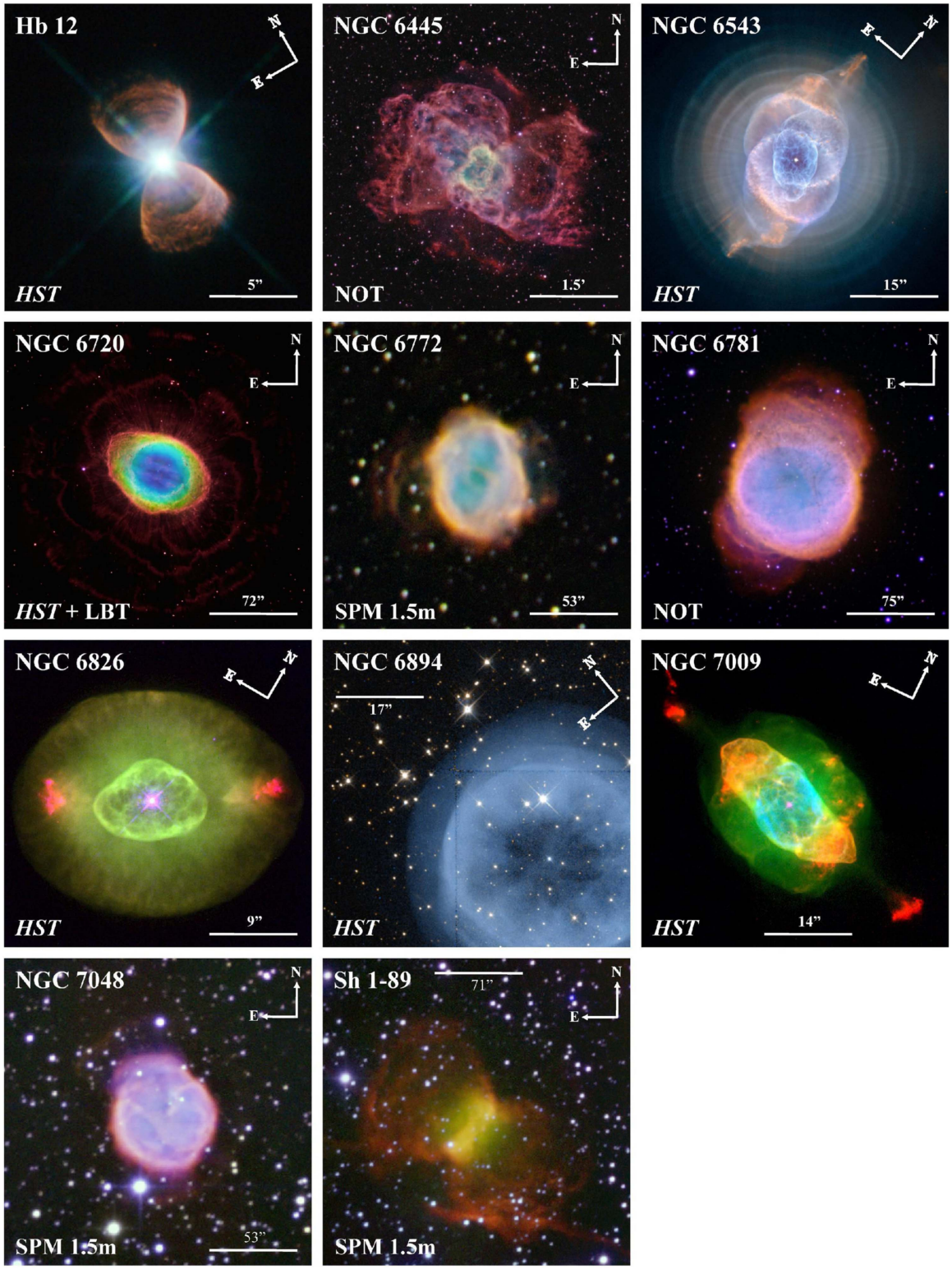

Figure 1. Color-composite optical images of our PN sample created with the [N II] (red), Hα (green), and [O III] (blue) images, except NGC 6894, which is combined from the *HST* WFC3 F814W (red) and F555W (blue) images. The telescopes used to obtain these images are indicated at the bottom left corner of each panel. Image scales and orientations are marked.

Space Telescope (MAST[12]) at the Space Telescope Science Institute. The *HST* optical images were obtained with the Wide-Field Planetary Camera 2 (WFPC2) and the Wide Field Camera 3 (WFC3) in conjunction with the F502N, F656N, and F658N narrowband filters. The unparalleled high spatial resolution of the WFPC2 ($0\farcs0396\,\mathrm{pixel}^{-1}$) and WFC3 ($0\farcs040\,\mathrm{pixel}^{-1}$) cameras enables detailed inspection of the microstructures of our targets, especially for the inner nebular

[12] http://archive.stsci.edu

Table 1
Target List

PN Name	PNG	R.A.[a] (J2000.0)	Decl.[a] (J2000.0)	Distance[b] (kpc)	z[c] (kpc)	Age (10^4 years)	Morphology/References
Hb 12	PN G111.8−02.8	23:26:14.81	+58:10:54.65	2.26	0.110	⋯	Bipolar/[1]
NGC 6445	PN G008.0+03.9	17:49:15.21	−20:00:34.50	1.38	0.094	5.5–6.0	Bipolar/[2]
NGC 6543	PN G096.4+29.9	17:58:33.41	+66:37:58.79	1.15	0.573	5.8–12.0	Elliptical[d]/[3], [4]
NGC 6720	PN G063.1+13.9	18:53:35.08	+33:01:45.03	0.92	0.221	2.3–4.6	Bipolar/Ellipsoidal?[e]/[5], [6], [7]
NGC 6772	PN G033.1−06.3	19:14:36.37	−02:42:25.04	1.31	0.144	3.2–7.3	Bipolar/[8]
NGC 6781	PN G041.8−02.9	19:18:28.08	+06:32:19.29	0.72	0.036	>2.9–7.0	Bipolar/[8], [9]
NGC 6826	PN G083.5+12.7	19:44:48.16	+50:31:30:33	1.40	0.307	⋯	Elliptical/[10]
NGC 6894	PN G069.4−02.6	20:16:23.96	+30:33:53.17	1.50	0.068	⋯	Round/[11]
NGC 7009	PN G037.7−34.5	21:04:10.88	−11:21:48.25	1.26	0.713	>3.6–8.9	Elliptical/[12]
NGC 7048	PN G088.7−01.6	21:14:15.22	+46:17:17.52	1.81	0.050	3.5–4.1	Bipolar/[13]
Sh 1-89	PN G089.8−00.6	21:14:07.63	+47:46:22.17	1.85	0.019	6.7–8.1	Bipolar/[14]

Notes.
[a] R.A. and decl. were all adopted from Kerber et al. (2003) except NGC 6445, whose coordinates were adopted from Loup et al. (1993).
[b] Distances are adopted from Frew et al. (2016).
[c] Height above the Galactic plane.
[d] The elliptical inner core seems to be nested inside two bubbles that join at a common waist (Balick & Hajian 2004).
[e] Still in debate. See discussion in Section 4.1.
References [1] Kwok & Hsia (2007); [2] Vázquez et al. (2004); [3] Balick (2004); [4] Balick & Hajian (2004); [5] Guerrero et al. (1997); [6] Kwok et al. (2008); [7] O'Dell et al. (2013); [8] Kastner et al. (1994); [9] Phillips et al. (2011); [10] Corradi et al. (2003); [11] Manchado et al. (1996); [12] Gonçalves et al. (2003); [13] Kastner et al. (1996); [14] Hua (1997).

regions, where the optical emission usually dominates. The *HST* color-composite images of our targets are presented in Figure 1.

In particular, for Hb 12 we also retrieved the WFC3 broadband F140W ($\lambda_c = 1.392\ \mu$m, $\Delta\lambda = 3840$ Å) near-IR images (obtained through the *HST* program 11552, PI: H. A. Bushouse) from the archive. In the near-IR channel, the WFC3 detector has a FoV of $136'' \times 136''$ with a pixel scale of $0.''13$. The nine F140W images of Hb 12 (an exposure of 2.93 s each) were first aligned according to the central star position and then combined to enhance the spatial sample and remove cosmic rays.

2.4. The Spitzer Archive Data

Where available, the archival *Spitzer Space Telescope* mid-IR images were also used for a comparison study of the PN morphologies. The *Spitzer* images were observed with the Infrared Array Camera (IRAC; Fazio et al. 2004) employing four filters: 3.6 μm ($\lambda_c = 3.550\ \mu$m, $\Delta\lambda = 0.75\ \mu$m), 4.5 μm ($\lambda_c = 4.493\ \mu$m, $\Delta\lambda = 1.901\ \mu$m), 5.8 μm ($\lambda_c = 5.731\ \mu$m, $\Delta\lambda = 1.425\ \mu$m), and 8 μm ($\lambda_c = 7.872\ \mu$m, $\Delta\lambda = 2.905\ \mu$m). The IRAC images have plate scales of $\sim 1.''6$–$1.''8$ pixel^{-1} in these four bands and have a FoV of $5.'2 \times 5.'2$. Images were downloaded from the NASA/IPAC Infrared Science Archive in the form of *Spitzer* Enhanced Imaging Products (SEIP).[13]

2.5. The WISE Images

In order to facilitate analysis of our sample, we downloaded near- and mid-IR images of the *Wide-field Infrared Survey Explorer* (*WISE*; Wright et al. 2010) mission from the NASA/IPAC Infrared Science Archive (IRSA).[14] *WISE* performs an all-sky survey at 3.4 μm (*W*1), 4.6 μm (*W*2), 12 μm (*W*3), and 22 μm (*W*4) with angle resolutions of $6.''1$, $6.''4$, $6.''5$, and $12.''0$, respectively. The *WISE* images in the former three bands are used in this work.

3. Results

The CFHT near-IR images of our sample PNe are displayed in Figure 2. The images of NGC 6445 are haunted by a very crowded stellar field and thus are not presented in grayscale as in Figure 2, but will be shown later as a color-composite picture in this paper. Some H_2 images show extended halo structures surrounding the central nebulae. Some of these structures generally trace the optical images, but others are detected for the first time. However, the WIRCam K_c ($\lambda_c = 2.218\ \mu$m, $\Delta\lambda = 0.033\ \mu$m) filter used in these observations also includes the 1−0 S(0) 2.223 μm and 2−1 S(1) 2.243 μm line emission of H_2; thus strictly speaking, it is not a true *K*-continuum filter that can be used to subtract from the H_2 2.122 μm image, as usually done in a conventional manner. That is why in the CFHT images of some of our targets, we also see K_c emission in the nebular halos where the H_2 emission was detected. The K_c images are thus not analyzed in this paper; neither are they displayed in Figure 2. In this section, we compare the CFHT images with the optical images obtained with the *HST* and the ground-based telescopes. Implications for wind–wind interaction as well as possible interactions between PNe and the ISM are discussed in Section 4.

3.1. Hb 12

Hb 12 has been classified as a PN by its emission line spectrum (e.g., Hyung & Aller 1996). Its compactness as well as high surface brightness in the IR (Zhang & Kwok 1990) and radio (Aaquist & Kwok 1990) emission indicates that it is a PN at an early stage of evolution, which is consistent with a very young kinematic age derived through high-resolution spectroscopy (Miranda & Solf 1989). Hb 12 has a well-defined hourglass shape in the *HST* optical narrowband

[13] http://irsa.ipac.caltech.edu/data/SPITZER/Enhanced/SEIP/
[14] http://irsa.ipac.caltech.edu/applications/wise

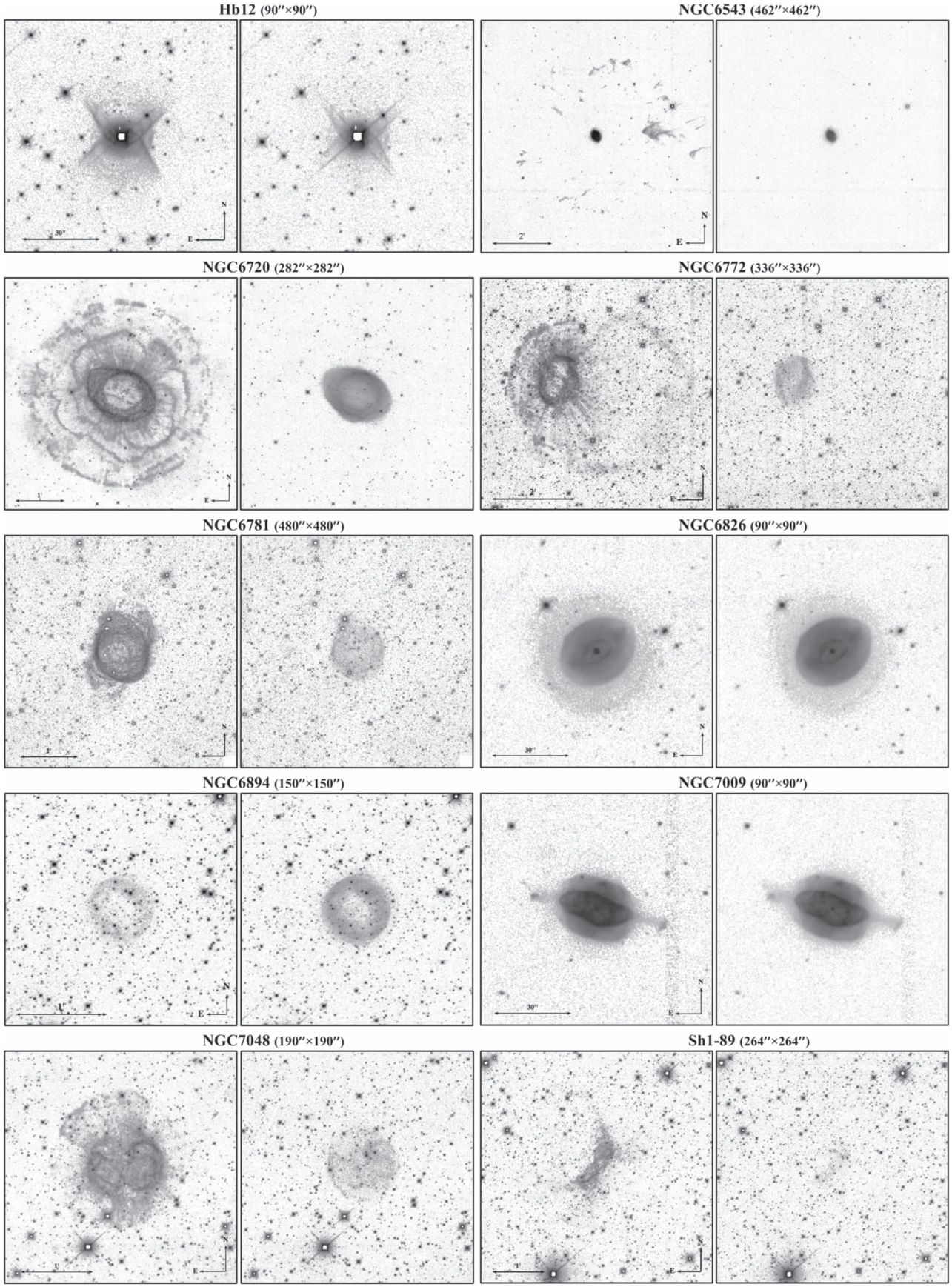

Figure 2. CFHT WIRCam negative grayscale images of our sample PNe. For each PN, the H_2 (left) and Brγ (right) images are displayed; target name and image size (in arcseconds) are indicated.

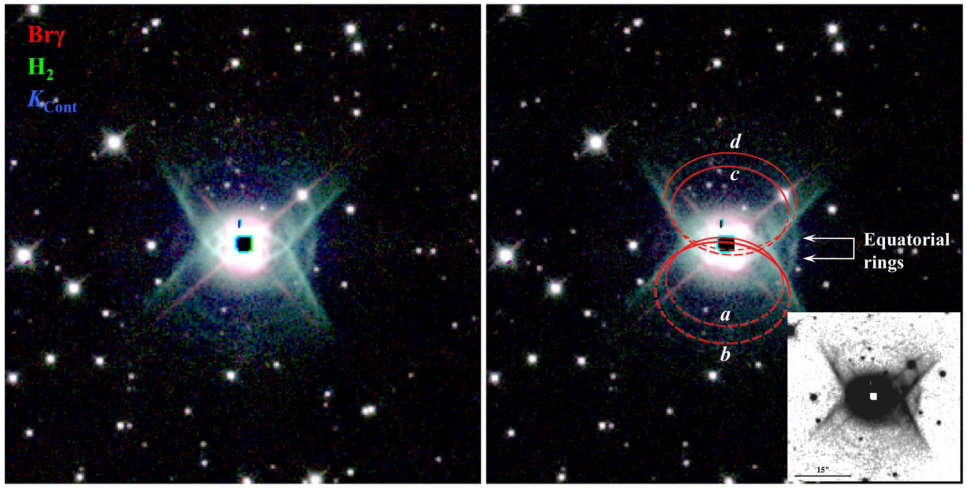

Figure 3. Left: CFHT color-composite image of Hb 12 created with the Brγ (red), H_2 (green), and K_c (blue) filters. Image size is similar to Figure 2. North is up and east to the left. Right: same as on the left but overplotted with schematic outlines of four coaxial rings (red ellipses); the front side of the red ellipses is solid and the back side is dashed. The inset shows the H_2 image scaled to show the rings.

images (Kwok & Hsia 2007). Spectroscopic observations in the H_2 emission indicate that a huge range of gas density (10^4–10^5 cm^{-3}) exists in this compact object (Ramsay et al. 1993). Optical spectroscopy also reveals electron density as high as ~500,000 cm^{-3} (Hyung & Aller 1996). Fluorescent molecular hydrogen emission was detected in the $<4''$ inner region of Hb 12 (Dinerstein et al. 1988). All these studies point to the peculiarity of this object.

Our CFHT images not only show bipolar lobes of Hb 12 but also reveal more detailed structures in H_2 emission. This is better seen in the color-composite image (Figure 3), where some arcs are seen aligned in the bipolar lobes. A close inspection of the image shows that there are two arcs in the southern lobe, while in the northern lobe, there also seem to be two arcs marginally visible. They are probably due to coaxial, concentric rings on either side of the central star, aligned along the bipolar lobes. These rings can generally be fitted by ellipses with a minor-to-major axis ratio of ~0.7. If we assume that the rings are circular, this ratio indicates a inclination angle (i.e., the angle of the polar axis with respect to the plane of the sky) of 45° ± 7°.

The two northern rings are about 0.106 and 0.119 pc, or ~21,860 and 24,500 au, respectively, from the central star. The two southern rings are 0.110 and 0.133 pc, corresponding to 22,750 and 27,420 au, respectively, from the central star. These distances of the rings have been corrected for the inclination angle (45°) of the polar axis, and a distance of 2.26 kpc (Cahn et al. 1992; Frew et al. 2016) to Hb 12 was assumed. The opening angle of the bipolar lobes in the H_2 emission is about 75°.

Kwok & Hsia (2007) proposed that the bipolar lobes of Hb 12 (observed by *HST* WFPC2) may represent an inner hourglass nested in a much larger bipolar structure, a morphology that is similar to some other hourglass-shaped bipolar nebulae such as the "Minkowski's Butterfly Nebula" M 2-9 (e.g., Castro-Carrizo et al. 2012, 2017), Hen 2-104 (Corradi et al. 2001), MyCn 18 (Bryce et al. 1997; Sahai et al. 1999), and SN 1987A (Panagia et al. 1996; Sugerman et al. 2005). Comparison of our CFHT images with the archival *HST* optical image indicates that Hb 12 does exhibit multiple bipolar lobes (Figure 4, left). Based on the fits of the multiple elliptical rings observed in the *HST* WFPC2 [N II] image, Kwok & Hsia (2007) derived an inclination angle of ~38° for the polar axis of Hb 12. This inclination angle is consistent with both the value of 40° derived by Hyung & Aller (1996) and ours (45° ± 7°) derived from the H_2 near-IR image. Thus the two pairs of bipolar lobes are aligned with each other, and the southern lobes are tilted toward the observer (Hyung & Aller 1996). The position angle (PA) of the axis of Hb 12's bipolar lobes is 171°.5 ± 2°.3 (Kwok & Hsia 2007). The arcs at the equatorial region that represent the outer bipolar lobes of Hb 12 (Figure 4, right) were also noticed in the *HST* NICMOS F212N image (Clark et al. 2014).

Between the outer bipolar lobes observed via H_2 emission and the primary lobes in *HST* F658N (Figure 4, left), there seems to be a third pair of bipolar lobes, which can be inferred from a smaller eye-shaped feature shown in the *HST* WFC3 F140W image (Figure 4, right). This pair of bipolar lobes, hereafter named as the inner lobes, is expected to be another hourglass structure located between the two more obvious lobes described above. This smaller eye-shaped feature, which is probably due to projection of the inner pair of bipolar lobes, can be marginally seen in the H_2 image and has been noted in the *HST* NICMOS F160W image (Kwok & Hsia 2007, Figure 2 therein).

Moreover, we found in the H_2 image two pairs of faint, point-symmetric knots along the polar axis of Hb 12 (Figure 5, marked as N1 and S1, and N2 and S2) with projected lengths of ~133″ and ~353″, respectively. The inner pair of knots (N1 and S1) was detected in [N II] (Vaytet et al. 2009), while the outer knots (N2 and S2) are new discoveries. The two pairs of knots have slightly different position angles, probably indicating this PN hosts a bipolar, rotating episodic jet (BRET; C.-H. Hsia et al., in preparation). These features were briefly reported in Hsia et al. (2016).

3.2. NGC 6445

NGC 6445 has been classified as a bipolar PN (e.g., Aller et al. 1973; Peimbert & Torres-Peimbert 1983; Perinotto 1991; Corradi & Schwarz 1995). Its He/H and N/O abundance ratios are consistent with the Type I definition (Peimbert & Torres-Peimbert 1983). Previous optical imagery of this PN reveals a bright, central ring-shaped morphology and open bipolar lobes

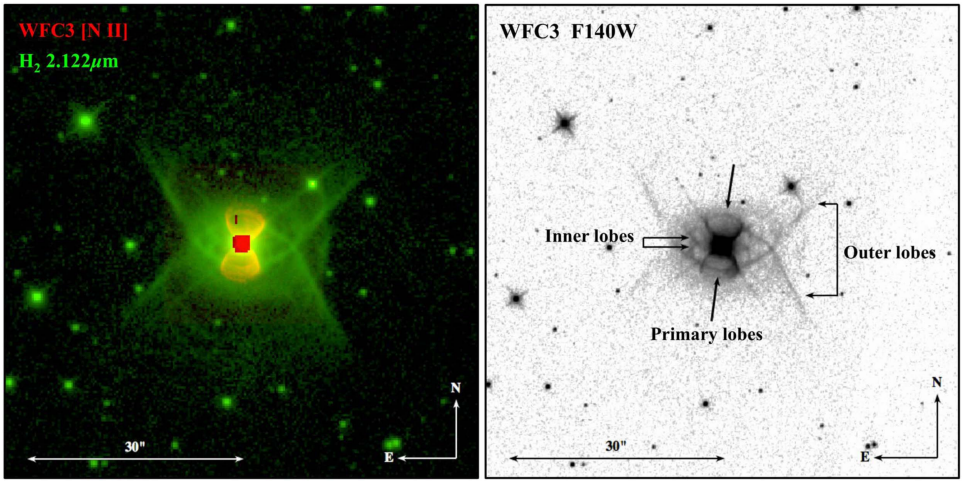

Figure 4. Left: color-composite image of Hb 12 created with the *HST* WFC3 F658N (red) and CFHT WIRCam H_2 (green) images. Right: *HST* WFC3 F140W image displayed in negative grayscale (*HST* program 11552, PI: H. A. Bushouse). The primary bipolar lobes of Hb 12 defined in the F140W image follow the [N II] morphology (left). Central arcs in the F140W image, probably due to projection of the inner and outer bipolar lobes, are also seen in the H_2 image.

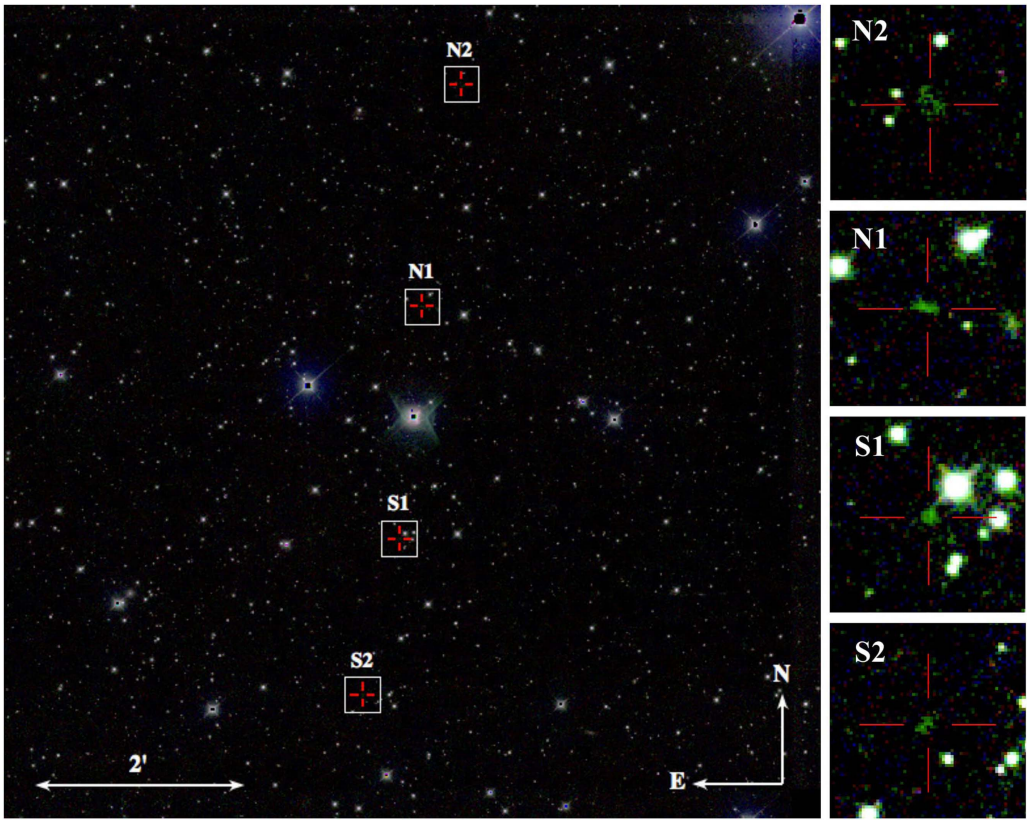

Figure 5. Same as Figure 3 but with a wider field centered on Hb 12. The two pairs of H_2-emitting knots, defined as S1 and N1 for the inner pair and S2 and N2 for the outer pair, are marked and zoomed-in in the right panels, each with a size of $20'' \times 20''$.

(van Hoof et al. 2000); the outer envelope emission of NGC 6445 is [N II]-dominant (Phillips & Ramos-Larios 2010). The physical structure and internal kinematics were studied by Vázquez et al. (2004). Despite these multiwavelength studies, the properties and exact structure of NGC 6445 are still poorly defined (Phillips & Ramos-Larios 2010). Our NOT ALFOSC wide-field optical images show that NGC 6445 has an irregularly shaped central region with a size of $\sim 40'' \times 50''$, where the [O III] emission dominates, while the [N II] emission is much more extended and defines an overall bipolar morphology (Figure 1). The bipolar lobes are along the east–west (EW) direction with PA $\sim 80°$, stretching to $\sim 1\farcm6$ from the center. There are also many filamentary structures across the nebula, which hint at a more complex morphology of NGC 6445 than previously claimed. The breadths of the EW lobes reach $\sim 1\farcm8$ at both ends.

Our CFHT WIRCam images of NGC 6445 show that the majority of the H_2 2.122 μm, Brγ 2.166 μm, and K_c 2.218 μm emission comes from its central region (Figure 6, left). There are very faint, extended structures in the H_2 emission, which are almost overwhelmed by bright field stars but are still marginally visible in the color-composite image, where the

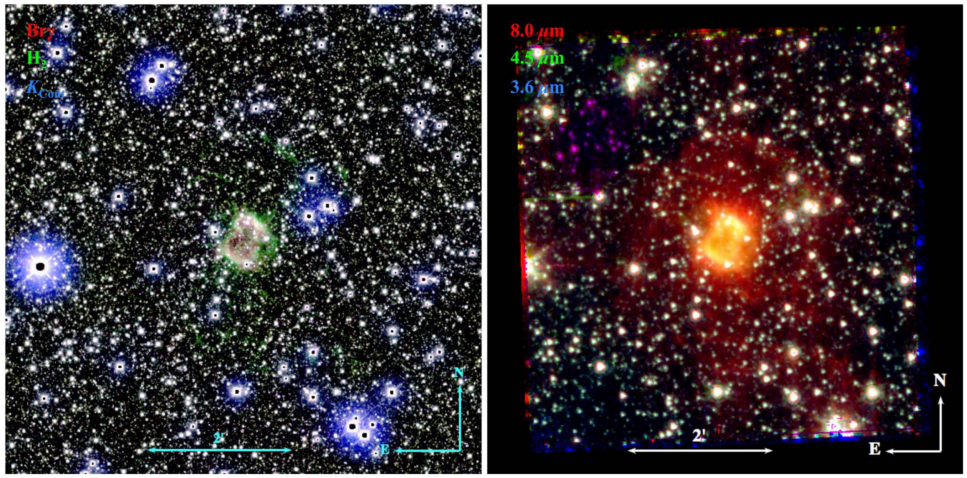

Figure 6. Left: CFHT color-composite image of NGC 6445; color code is indicated. Right: *Spitzer* color-composite image of NGC 6445 created with the IRAC 3.6 μm (blue), 4.5 μm (green), and 8.0 μm (red) bands. Image size and orientation are the same as in the left panel.

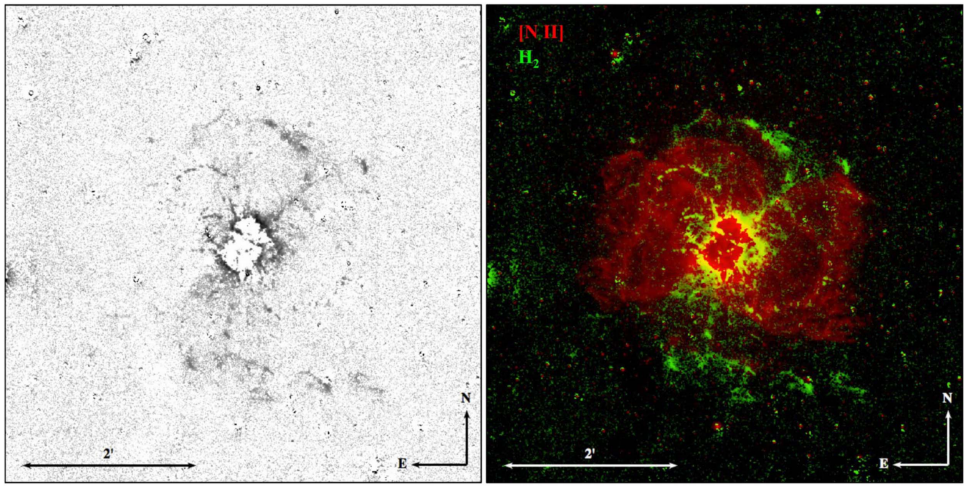

Figure 7. Left: residual H_2 image of NGC 6445 created by subtracting the scaled Brγ image from the H_2 image. Right: color-composite image of NGC 6445 created with the [N II] (red) and the residual H_2 (green) images.

extended H_2 emission seems to be limb-brightened. The *Spitzer* mid-IR images show that NGC 6445 is more extended in the 8.0 μm emission (Phillips & Ramos-Larios 2010), which fills the halo region defined by the seemingly limb-brightened H_2 emission (Figure 6, right).

In order to alleviate the effects of the dense stellar field and better show the faint halo in H_2, we created a residual image of NGC 6445 by subtracting the scaled Brγ image from H_2. This residual image is expected to be in H_2 emission only and shows filamentary features well outside the central region along the north–south (NS) direction (Figure 7, left). These filaments are located $\sim$1.′3–1.′6 from the center. The southern filaments are more extended along the EW direction. There are also rays of faint emission coming from the central region. The factor used to scale the Brγ image was carefully chosen so that emissions of stars are mostly removed, and the nebular structures are best seen in the residual image.

We are aware that (1) it is dangerous to subtract the Brγ emission from the H_2 image because H_2 may be partially removed if it is spatially coincident with Brγ, and (2) it is conventional to subtract the *K*-continuum emission from the H_2 image. However, our main purpose is to search for nebular structures in H_2 emission in the outer reaches of previously know PNe; besides, the Brγ emission is mostly present in the inner nebulae and is much fainter in the outer halos where the H_2 emission is detected. As mentioned at the beginning of Section 3, the K_c filter of WIRCam does not cover the real continuum but includes the 1−0 S(0) and 2−1 S(1) emission lines of H_2. It is thus even more dangerous to subtract the K_c image from the H_2 if one wants to study the extended structures in the H_2 emission.

A close comparison of the residual H_2 image against the *Spitzer* IRAC 8.0 μm and the NOT ALFOSC [N II] images shows that along NS the H_2 emission generally delineates the outer boundary of a broad region where the 8.0 μm emission dominates (Figure 6, right), while the [N II] emission is more extended along the EW direction, consistent with the bipolar morphology, and is confined within the 8.0 μm-emitting region along the NS. Along the NS direction, the H_2 emission appears to be slightly farther out than the [N II] emission (Figure 7). This reinforces the notion that the optical emission may be significantly affected by the illumination of UV photons and cannot represent the intrinsic matter distribution of PNe (e.g., Zhang et al. 2012c). The [N II] image mainly traces the bipolar lobes, while the H_2 image reveals the limb-brightened gas extended along the equatorial direction.

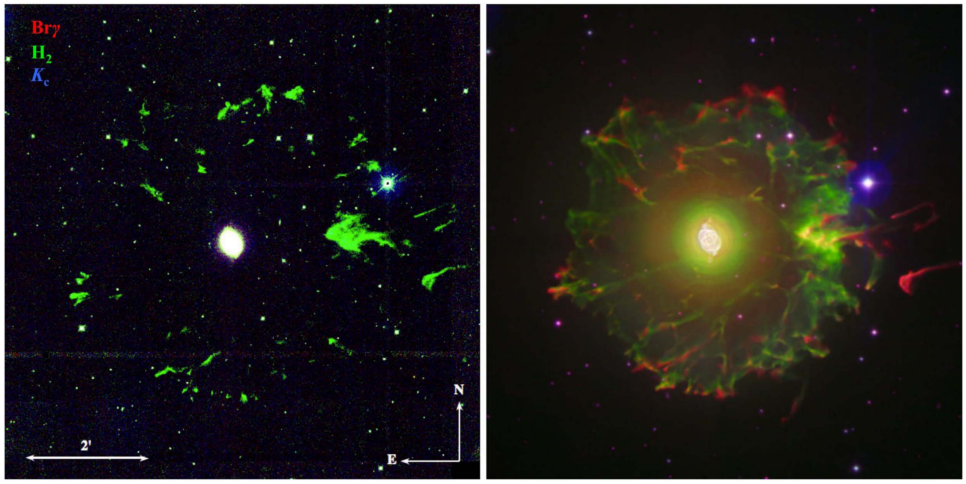

Figure 8. Left: CFHT color-composite image of NGC 6543. Right: optical image of NGC 6543 obtained from the 2.5 m Isaac Newton Telescope; adopted from the Isaac Newton Group of Telescopes (http://www.ing.iac.es/PR/press; image credit: D. López); red is the [S II] line emission, green is Hα, and blue is [O III]. Image size and orientation are the same as on the left.

The northern and the southern H_2-emitting filaments, ∼1.′4–1.′6 from the center of NGC 6445, might be the outer boundaries of an edge-on-viewed torus of this PN. This torus was ejected in the AGB phase and is now being disrupted by interaction with the fast stellar wind that was developed later. The south region of the torus seems to be much more disrupted than its north counterpart. Within the EW bipolar lobes, there seem to be two arcs in the H_2 emission, as shown in the residual image (Figure 7): a northeast (NE) arc and a southwest (SW) one, both ∼1.′0 from the nebular center. The SW arc seems to be disrupted but matches the position of a giant arc in [N II]. These two H_2 arcs might define another pair of bipolar lobes, which have a PA ∼ 56°. This PA generally agrees with that of the [O III]-right inner nebular region of NGC 6445 (Figure 1), suggesting that the smaller bipolar bubbles are of relatively higher excitation and thus might have developed recently.

3.3. NGC 6543

Morphological and structural studies of NGC 6543 (a.k.a. the Cat's Eye Nebula) based on the optical images have been carried out extensively (e.g., Balick et al. 1992; Harrington & Borkowski 1994; Reed et al. 1999; Corradi et al. 2003; Balick 2004; Balick & Hajian 2004). A giant (angular diameter ∼300″) patchy/filamentary outer halo has previously been discovered beyond the bright core in the optical wave bands (Millikan 1974; Middlemass et al. 1989; Balick et al. 1992). The *HST* imagery revealed regularly spaced, concentric circular rings surrounding the bright core (Figure 1), which were explained as spherical bubbles of periodic isotropic mass pulsations that preceded the formation of the bright nebular core (Balick et al. 2001).

Our CFHT near-IR images show that the giant halo surrounding the Cat's Eye is dominated by H_2 emission (Figure 8, left), which generally follows [S II] that delineates the outer edges of the knotty/filamentary features (Figure 8, right); the morphologies of the H_2 features also follow the fine structures observed in Hα + [N II] (Balick et al. 1992, Figure 4 therein), except that the halo seems smoother in the latter broadband filter. This morphology indicates that H_2 (and also [S II]) may be shock excited. Previous optical spectroscopy found that the [O III] electron temperature of the faint halo of NGC 6543 is higher than that of the bright central core; this was proposed to be due to hot, fast stellar wind that escaped from the central nebula and shocked the filamentary halo (Middlemass et al. 1989, 1991; Meaburn et al. 1992). This fast wind mass-loads as it penetrates the central nebula, resulting in a mildly supersonic flow that shocks the clumps of material in the halo region (Dyson 1992). The halo is also observable in *Spitzer* (Figure 9). The spatial distribution of dust emission resembles that of H_2. It is still unclear whether there is relevance between the halo and the concentric circular rings around the inner Cat's Eye (Figure 1).

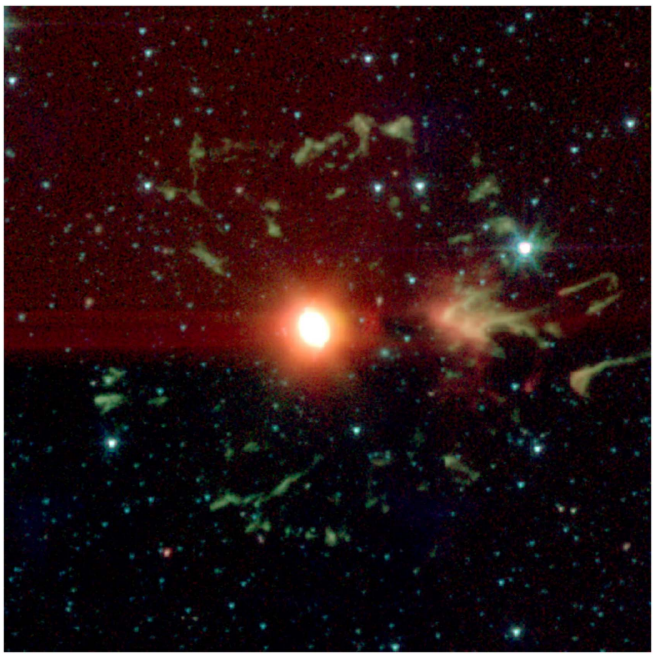

Figure 9. *Spitzer* color-composite image of NGC 6543 created with the IRAC 3.6 μm (blue), 4.5 μm (green), and 8.0 μm (red) bands. Image size and orientation are the same as in Figure 8.

The filamentary outer halo of NGC 6543 was observed to be detached from the concentric rings around the bright inner Cat's Eye, indicating that the halo material was probably

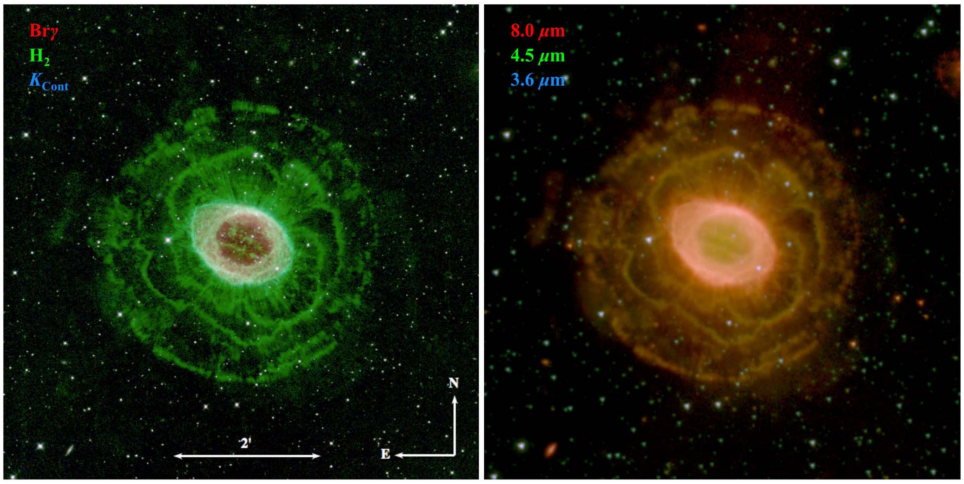

Figure 10. Left: CFHT color-composite image of NGC 6720. Right: *Spitzer* IRAC color-composite image; image size and orientation are the same as on the left.

ejected well before the periodic ejection of the spherical gas. The average kinematic age of this giant halo, as computed assuming a constant expansion velocity, is ∼85,000 years (Corradi et al. 2003). Based on the spacing between the concentric rings and an assumption of constant expansion velocity ($10\,\mathrm{km\,s^{-1}}$), Balick et al. (2001) estimated that launching of the spherical bubbles from the surface of the progenitor star began about 15,000 years ago. For comparison, the expansion age of the inner nebula is ∼1000 years (Reed et al. 1999). Such a huge difference in the kinematic ages of the giant halo and the circular rings indicates that these two structural components could be ejected at different episodes during the evolution from the late-AGB to the PN phase.

3.4. NGC 6720

The halo around NGC 6720 (a.k.a. the Ring Nebula) has been observed in the optical emission (e.g., Balick et al. 1992; Corradi et al. 2003) and IR emission lines of molecular hydrogen (e.g., Beckwith et al. 1978) and CO (e.g., Huggins & Healy 1986). The central star of NGC 6720 has exhausted the hydrogen shell burning and is now on the cooling track. Thus the outer halo of NGC 6720 is recombining. The *Herschel* far-IR observations reveal a resemblance between the dust distribution and the H_2 emission in the inner nebula, suggesting that H_2 forms on grain surfaces (van Hoof et al. 2010).

There are structures in the halo of NGC 6720: the two inner layers have petal-like morphologies, while the outermost one is almost circular. These features, together with the radial filaments emerging from the central nebula, point to a possibility that the recombining halo of NGC 6720 might be in the process of disruption due to interaction with the stellar wind. The halo is dominated in the H_2 emission and also visible in K_c; this may imply a relatively low H_2 1−0 S(1) to H_2 2−1 S(1) line ratio, but it is difficult to resolve quantitatively because of many contributions (from stellar continuum, dust continuum, and H_2 lines) to this K_c filter. If the H_2 1−0 S(1)/2 −1 S(1) ratio is indeed low in the halo of NGC 6720, its H_2 emission is then likely due to UV pumping (e.g., Marquez-Lugo et al. 2015), especially for the petal-like features of the inner halo that disclose regions where UV photons escape from the core region. The *Spitzer* IRAC near-IR images show that the $\sim 60'' \times 88''$ ellipse-shaped inner region of NGC 6720 is very bright in the 8.0 μm emission. The 8.0 μm emission in the outer halos is also stronger than the other three IRAC bands (Figure 10, right).

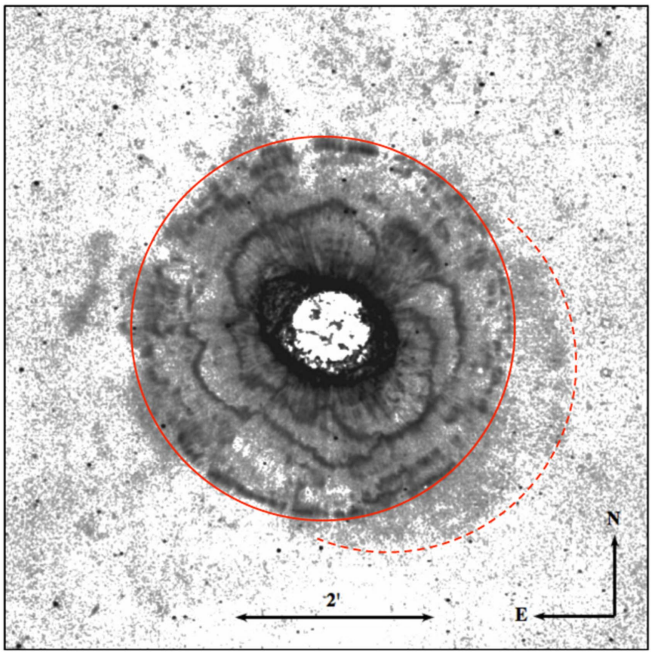

Figure 11. Residual image of NGC 6720 created by subtracting the scaled Brγ image from the H_2 image. The central region is saturated to enhance the extended structure. The red solid circle is a schematic fit to the ∼2′ radius outer halo, and the red dashed arc delineates the faint southwest crescent.

We created a residual image of NGC 6720 using the same method as we did for NGC 6445 (Section 3.2) to enhance the extended morphologies in H_2. The radial filaments, pointing away from the central ring and penetrating the inner (petal-like) halo, are clearly visible in Figure 11. Besides, a crescent-shaped structure was found attached to the southwest of the circular outer halo; this might be due to inclination of the bipolar lobes of NGC 6720, as suggested by Kastner et al. (1996). Kwok et al. (2008) speculate a triple biconic structure of the outer halos of NGC 6720.

An alternative model was proposed by Guerrero et al. (1997, Figure 14 therein), who, through high-dispersion spectroscopy, suggested that the bright ring of NGC 6720 is actually a closed shell with a prolate ellipsoidal geometry with density

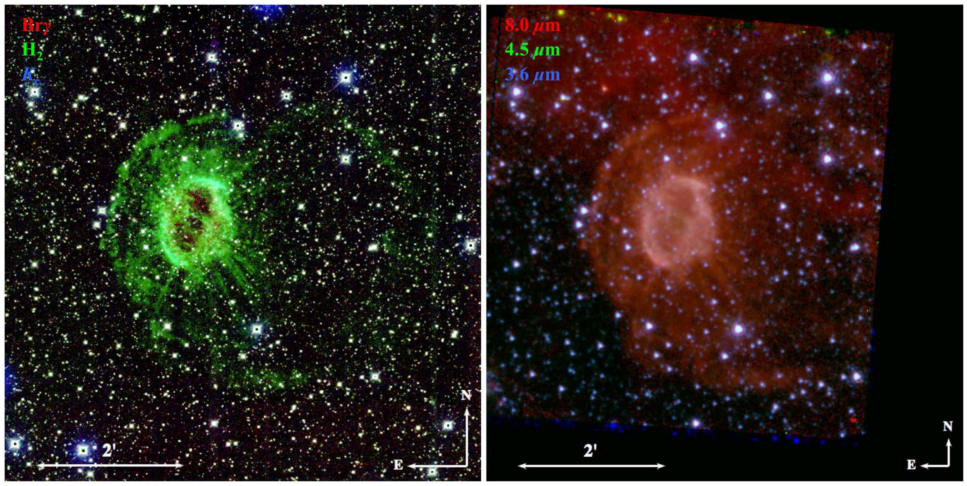

Figure 12. Left: CFHT color-composite image of NGC 6772. Right: *Spitzer* IRAC color-composite image; image size and orientation are the same as on the left.

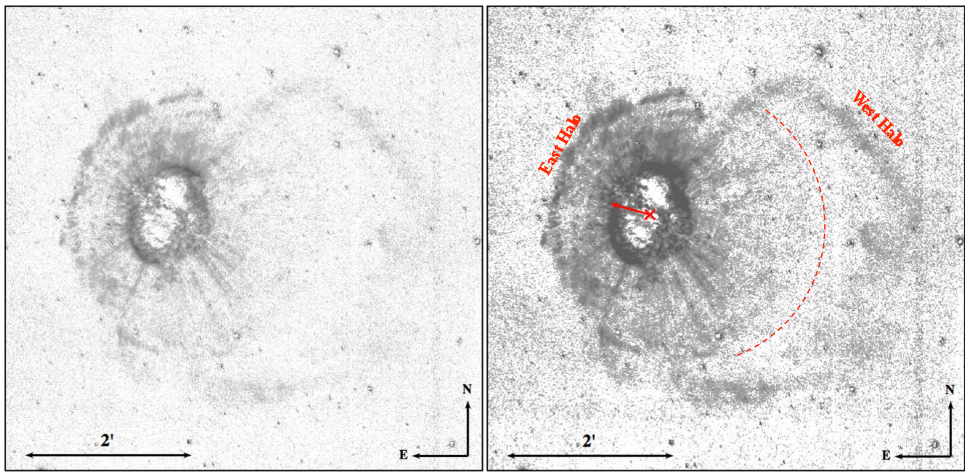

Figure 13. Left: residual image of NGC 6772 created by subtracting the scaled Brγ image from the H_2 image. Right: same as left but with a different cut level and slightly Gaussian smoothed to enhance the extended halo structure. The east and west halos may originally belong to the same circular outer halo. The red dashed arc roughly delineates the boundary of the disrupted inner halo. The red cross marks the central star position, and the red arrow with PA = 77° indicates the possible direction of proper motion.

enhancement near the equator, and surrounding this inner shell there is a halo of remnant red giant wind. Based on the *HST* imaging, O'Dell et al. (2013, Figure 11 therein) suggested that the main ring of NGC 6720 is an ionization-bounded disk with a central cavity and perpendicular extended lobes pointed nearly along the line of sight. Detailed morphokinematic analysis with the aid of models is needed to assess these three interpretations of NGC 6720's intrinsic structure.

3.5. NGC 6772

NGC 6772 has an obviously asymmetric halo in H_2 emission that is invisible in Brγ (Figure 2). This halo is better shown in Figure 12 (left), where we can see that H_2 emission dominates the halo, while Brγ only comes from the inner region. The H_2 emission is mainly concentrated on the inner nebular shell, which has a size of $\sim 28'' \times 37''$ and is slightly tilted (with PA $\sim$ 165°). The distribution of Brγ emission is more homogeneous within the nebular shell and is well consistent with Hα (Figure 1). It is interesting to note that H_2 generally traces [N II]: they both mainly come from the inner shell. Within this shell, there are also some H_2 filaments that seem to be also present in the [N II] image.

Although previously studied in the mid- and near-IR (including the H_2 2.122 μm line; e.g., Webster et al. 1988; Kastner et al. 1994; Ramos-Larios & Phillips 2009; Marquez-Lugo et al. 2013), the complete morphology of NGC 6772's halo is so far only displayed in our CFHT images. The *Spitzer* IRAC imaging reported in the literature does not cover the whole SW halo of NGC 6772 (Figure 12, right). The *Spitzer* 8.0 μm emission generally traces the extended halo of NGC 6772, but its spatial resolution is much lower than our CFHT WIRCam images.

In the residual H_2 image of NGC 6772 (Figure 13), we found that the eastern halo, although slightly fragmented, is overall bow-shaped, and its outer boundary is $\sim$75″–80″ from the central star, while the western halo seems to have been disrupted and extends as far as $\sim 3\farcm2$ from the central star. This morphology indicates that NGC 6772 might be interacting with the ISM. NGC 6772 thus best shows the possible PN–ISM interaction among our sample. According to the morphology of the extended halo, we conclude that this PN may have a proper motion with respect to the local ISM at PA $\sim$ 77° (Figure 13, right). In the H_2 image of NGC 6772, there are numerous radial filaments or rays coming out from the inner shell (or the inner

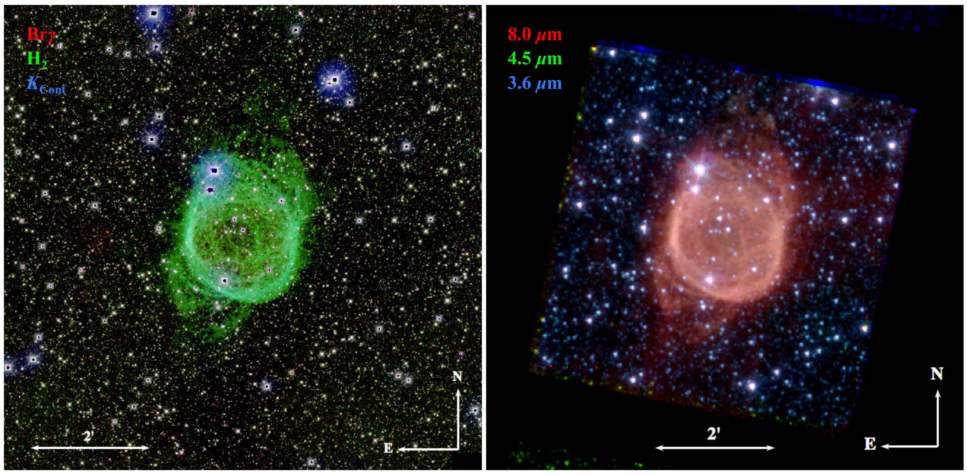

Figure 14. Left: CFHT color-composite image of NGC 6781. Right: *Spitzer* IRAC color-composite image; image size and orientation are the same as on the left.

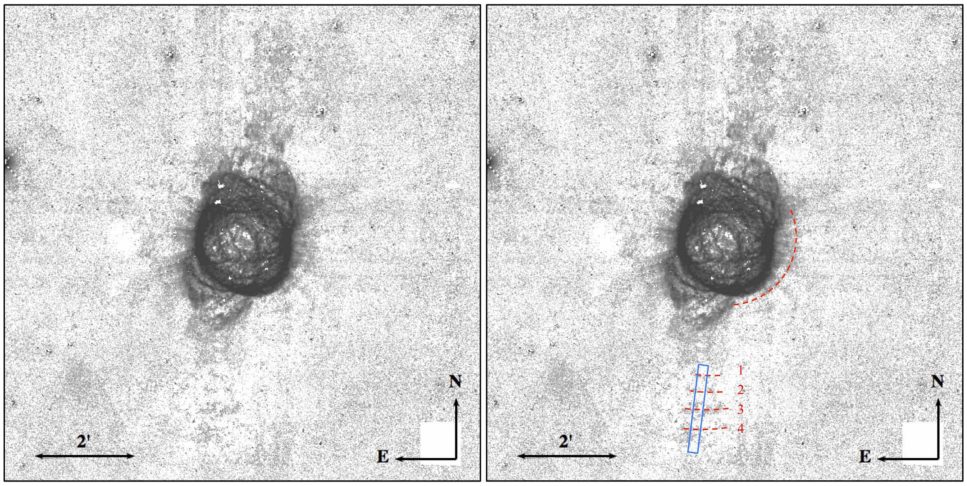

Figure 15. Left: residual image of NGC 6781 created by subtracting the scaled Brγ image from the H_2 image and then slightly Gaussian smoothed to reduce noise. The central nebula/ring is slightly saturated to enhance the extended structure. Right: same as the left panel but overplotted with a schematic sketch of possible rings (red dashed curves; see the text for description). The blue rectangle is a cut through the four possible rings as labeled with numbers.

ring) pointing toward the outer halo; they might be shadows from the clumps in the inner shell. Such radial features are also seen in several other PNe, most obviously in NGC 6720 (Figures 10 and 11).

3.6. NGC 6781

Optical images of NGC 6781 obtained in [O III], Hα, and [N II] (Figure 1) show a slightly elliptical, [O III]-luminous inner region with a radius of $\sim$50″ and an extended nebular structure along the NS direction, where [N II] emission is dominant. The inner nebular shell is also enhanced in [N II] emission. This morphology was observed by Phillips et al. (2011), who studied this PN using the NOT+*HST* images as well as the *Spitzer* mid-IR and *ISO* near-IR data.

Our deep H_2 2.122 μm image shows that NGC 6781 has a slightly ellipse-shaped central nebula and extended nebular structures along PA $\sim$ 120° (Figure 14). There are a series of arcs along the south extended region, with their intensities decreasing farther out. The northern extended structure is more diffuse than its southern counterpart. This morphology is generally consistent with the [N II] image. More details are clearly revealed for the inner region by our high-resolution image: there are many filamentary fine structures in the inner nebula, and the H_2 emission is enhanced at the outer boundary. The much weaker Brγ emission mainly comes from the central region and has a more homogeneous distribution; the K_c emission, although weaker, shows a morphology similar to that seen in H_2. In general, H_2 is the dominant emission among the CFHT near-IR bands utilized in our observations and delineates the main structure of NGC 6781.

In order to remove background stars and search for possible extended structures of NGC 6781, we created a residual image of NGC 6781 (Figure 15). In this "cleaned" residual H_2 image, we see many radial filaments coming out from the central nebula/ring, features also seen in NGC 6720 and NGC 6772 (Figures 10–13). Very close to the inner nebula, there seems to be a faint ring in the SW (Figure 15), which is $\sim$1.′37 from the center of the PN. In the south halo, we found very faint "ripples" that are $\sim$2.′7, 3.′0, 3.′35, and 3.′75 from the center of the nebula (Figure 15, right). These faint features might be part of the concentric rings in the halo of NGC 6781. Although the signal-to-noise ratio (S/N) is low, a radial cut through this region does show four peaks (Figure 16). We did not see any northern counterparts of these faint ripples.

The morphology of the inner nebular ring of NGC 6781, as well as the SE H_2 arcs, has been explained as projected

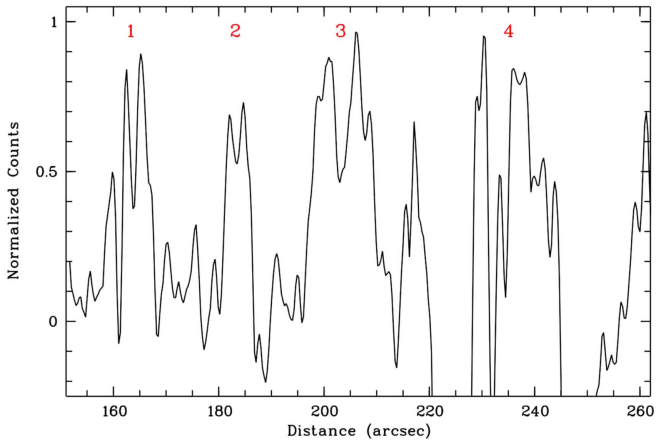

Figure 16. Radial profile of the cut through the southern halo of NGC 6781 (the blue rectangle in Figure 15). Approximate peak positions of the four possible southern rings (labeled with numbers in Figure 15, right) are marked with corresponding numbers. Horizontal axis is the distance (in arcseconds) from the central star.

cylindrical cavities (Kastner et al. 1994). In order to explain the kinematic structure of NGC 6781 observed through high-resolution spectroscopy of the H_2 2.122 μm emission line, Hiriart (2005) also suggested a thin, hollow cylindrical shell whose axis is tilted with respect to the line of sight. The faint features discovered in the extended halo may help to constrain the 3D structure of NGC 6781 and shed light on the history of the fast stellar wind and the material expelled in the AGB phase.

3.7. NGC 6826

An extended halo, nearly twice the radius of the ellipse-shaped inner nebula, has been noticed in the optical images of NGC 6826 (Balick et al. 1992; Corradi et al. 2003). A faint, round halo can also be seen in all CFHT filters; it has a sharp boundary extending to $\sim$25″ from the central star (Figure 17). The ellipse-shaped inner nebula, as defined in the optical bands (Figure 1), is bright in the Brγ emission.

3.8. NGC 6894

No extended nebular structures were found in the halo of NGC 6894 in our CFHT images (Figure 2). The main nebula shell, which has an outer radius of $\sim$24″, is dominated by the Brγ emission (Figure 18). There is a nonspherical central hollow, which is elongated along PA $\sim$ 35°. The *HST* broadband image (Figure 1) shows that there seems to be a ring of halo surrounding the main nebula and extending to the same size as the CFHT WIRCam images. It is worth mentioning that some detached tail-like ISM material close to NGC 6894 was found (Chu et al. 1987). It was suggested that the halo of NGC 6894 might have been stripped by the ISM (Soker & Zucker 1997).

3.9. NGC 7009

The two well-known [N II]-bright outer knots are also enhanced in H_2 emission. We also see faint K_c emission in these two knots, which might be due to H_2 1−0 S(0) and/or H_2 2−1 S(1). The H_2 emission on the two knots is located farther out than that of Brγ, which is better seen in Figure 19. A very faint, extended [O III]-emitting halo was first detected by

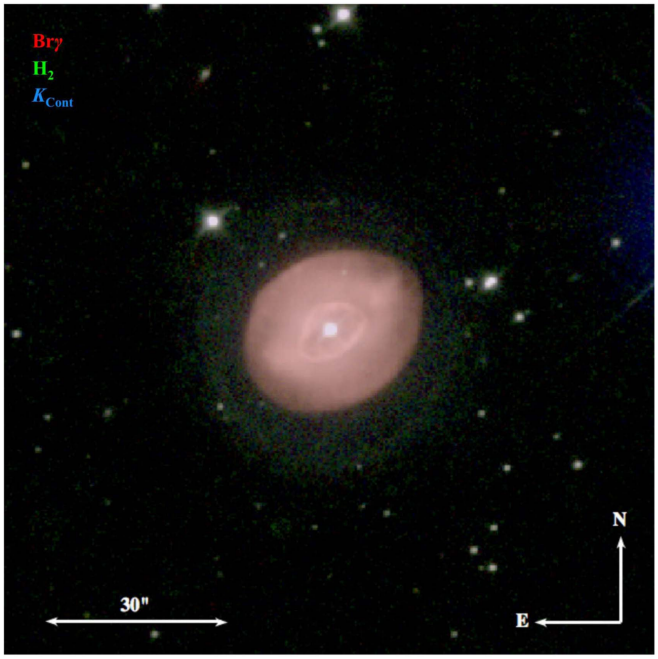

Figure 17. CFHT color-composite image of NGC 6826.

Moreno-Corral et al. (1998); its average surface brightness was later measured to be $\lesssim$0.02 of the central bright core (Corradi et al. 2003). The eastern part of the halo is semicircular, while the western halo is fragmented and filamentary. Through careful inspection of the CFHT images, we discovered in H_2 a number of knots and filamentary features surrounding the inner bright nebula (Figure 20). These condensations extend as far as $\sim$2′ from the central star and lie within the previously observed [O III] halo. The H_2 condensations are mostly distributed along the EW direction. The knots and filaments in the western halo are more elongated, while the eastern knots seem to be more compact. Some H_2 filaments in the western halo are nearly 10″ in length (Figure 20).

3.10. NGC 7048

Despite its brightness, the exact structure of NGC 7048 is yet to be investigated in detail. Our optical image (Figure 1) shows an almost round nebula with a radius of $\sim$32″. There seem to be two openings oriented at PA $\sim$ 15°, with the northern opening wider than the southern one. The [N II] emission is enhanced at the central nebula/shell, while Hα emission is more homogeneous. There are extremely faint extensions along the NS direction. Our CFHT images reveal an extended halo dominated by the H_2 emission (Figure 2). The Brγ emission is confined within the nebular shell. The IRAC 8.0 μm emission traces regions similar to H_2 but is more homogeneous (Figure 21).

The morphology of NGC 7048's halo is well demonstrated in the residual H_2 image (Figure 22). This halo has an overall round shape with slight deformation. The inner nebula/shell is displaced southward from the geometric center of the halo. The halo emission is inhomogeneous: H_2 emission is in the form of radial filaments coming out from the central shell, which resembles what is observed in NGC 6720. What is more intriguing is that the H_2 emission is stronger in the NS regions of the halo than in the EW. This seems to be in accordance with the opening direction of the central nebula in the optical image.

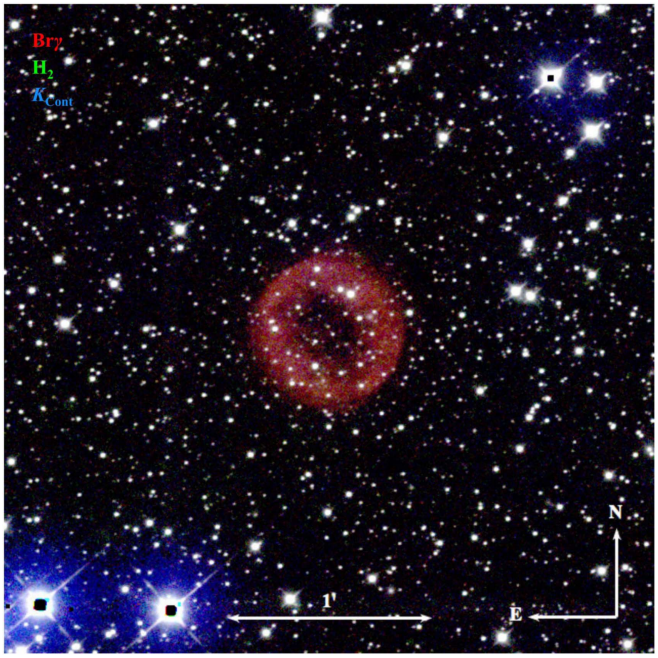

Figure 18. CFHT color-composite image of NGC 6894.

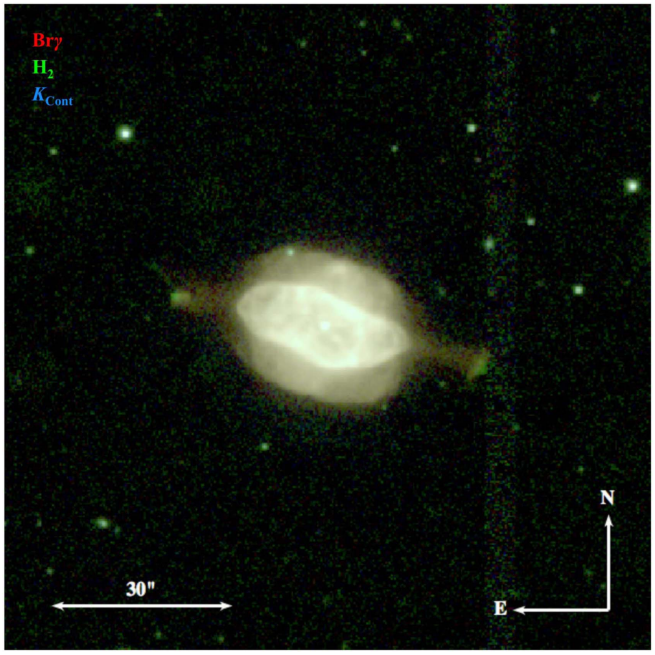

Figure 19. CFHT color-composite image of NGC 7009. The two EW knots are enhanced in H_2 emission.

Our CFHT H_2 image also reveals an approximately ∞-shaped feature along with numerous knots in the nebular center. The shape development of the outer halo is probably related to the central region. A detailed morphokinematic study of this PN is needed.

3.11. Sh 1-89

Sh 1-89 is a bipolar PN, as seen in deep optical images (Corradi & Schwarz 1995; Manchado et al. 1996; Hua 1997; Bohigas 2003). In the optical image, Sh 1-89 comprises a seemingly edge-on waist and a pair of bipolar lobes oriented along PA $\sim 48^\circ$ (Figure 1). The two lobes are dominated by the [N II] emission, which defines outer boundaries of the equatorial waist as well as the lobes. The [O III] emission mainly comes from the central region, while the Hα emission is more diffuse. In the south region of Sh 1-89, $\sim$1.′1 from the central core region, a giant filament dominates the [N II] emission, stretching by nearly 2.′8 along the EW direction and intersecting with the SW lobe. If this filament does not belong to Sh 1-89, it might be due to interaction with the ISM.

Our high-resolution near-IR images revealed very fine structures in the central region of Sh 1-89 (Figure 2). The central waist is torus-like, dominant in H_2 emission, and filamentary (Figure 23). The Brγ emission is faint. The residual H_2 image clearly shows that the central torus of Sh 1-89 is a tilted ring (Figure 24). This ring, with an angular diameter of $\sim$1′, has an apparent minor-to-major axis ratio of 0.189, corresponding to an inclination angle of $\sim$79° with respect to the line of sight, if we assume that the ring is circular. Previous H_2 imagery vaguely shows a tilted ring-like torus (Kastner et al. 1996), while our deep images confirm this morphology with much greater detail. There is extended H_2 emission beyond the central torus, which defines the boundaries of the bipolar lobes of Sh 1-89. There are also some ripple-like structures on both sides of the torus, along the NS direction, aligned with respect to the plane of the ring (Figure 24). These "ripples" in the H_2 line emission are probably some projected rings on the bipolar lobes of Sh 1-89, similar to Hb 12 (Kwok & Hsia 2007). Note that in the optical image, there are some diffuse ripples in the lobes in [N II] (Figure 1).

4. Discussion

4.1. H_2 Emission and Bipolarity

Detection of the molecular gas, most prominently H_2 and CO, toward PNe revealed that a significant fraction of nebular material is in molecular form and has led to new interpretations of their structures and evolution (e.g., Isaacman 1984; Storey 1984; Storey et al. 1987; Huggins & Healy 1986, 1989; Huggins et al. 1996). The association between H_2 emission and the bipolar morphology of PNe was discussed by Kastner et al. (1994, 1996), who defined the so-called *Gatley's rule*, which was later confirmed by a number of imaging surveys (e.g., Hora & Latter 1996; Hora et al. 1999; Guerrero et al. 2000; Marquez-Lugo et al. 2013). It also has been suggested that bipolar PNe evolved from the more massive low- and intermediate-mass stars ($\gtrsim$1.5–2.0 $M_\odot$; e.g., Peimbert & Torres-Peimbert 1983; Corradi & Schwarz 1995). However, as revealed by sensitive observations, H_2 emission also exists in PNe whose morphologies cannot be described as bipolar, but rather as ellipsoidal or barrel-like (Marquez-Lugo et al. 2013; Akras et al. 2017), suggesting that the detection of H_2 emission is not exclusive of bipolar PNe.

The standard definition of "bipolar" is largely based on the apparent morphologies of PNe (e.g., Corradi & Schwarz 1995). The bipolar PNe were grouped into two main subclasses: those with pinched equatorial waists ("bow-ties" or "hourglasses") and those with broad equatorial rings ("butterflies"; Marquez-Lugo et al. 2015; Ramos-Larios et al. 2017). These two groups of nebulae were previously called the early and late butterfly types, respectively, and were even proposed to be two phases of an evolutionary sequence (Balick 1987), although this postulation is disputed (Ramos-Larios et al. 2017).

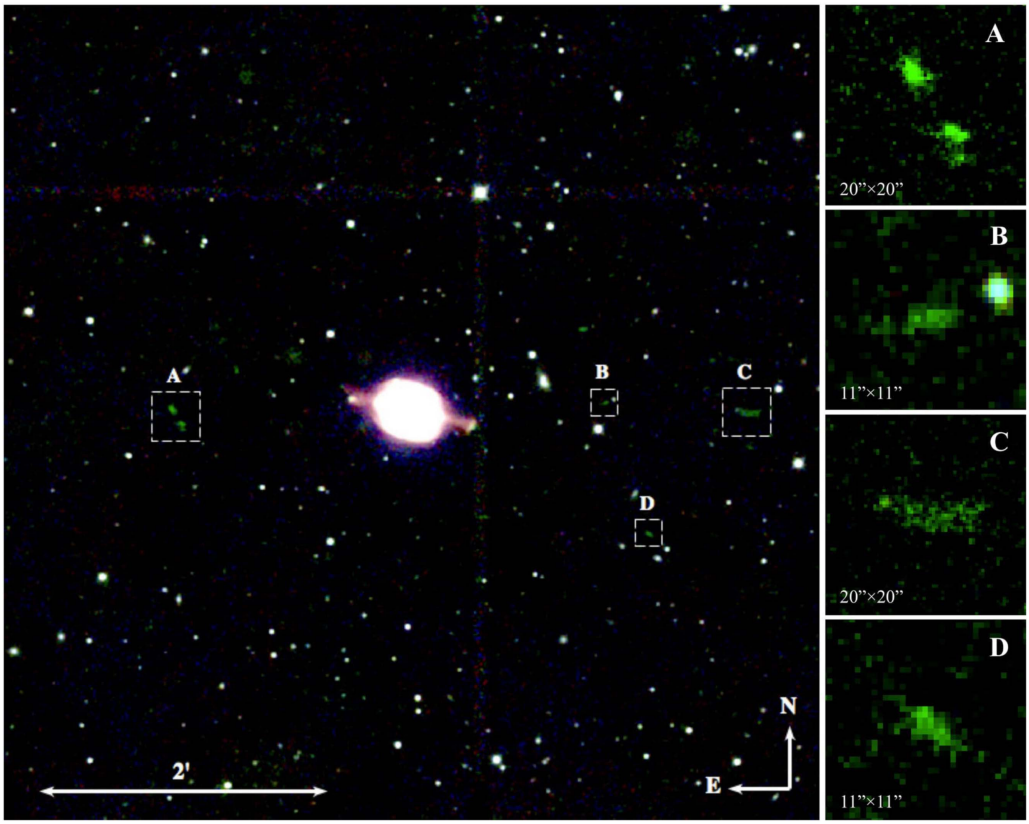

Figure 20. Same as Figure 19 but with a much wider field centered on NGC 7009. The central nebula is saturated so that the faint knots and filaments in the halo are visible in H_2 (green). Some halo features (marked as A, B, C, and D) are zoomed-in in the right panels.

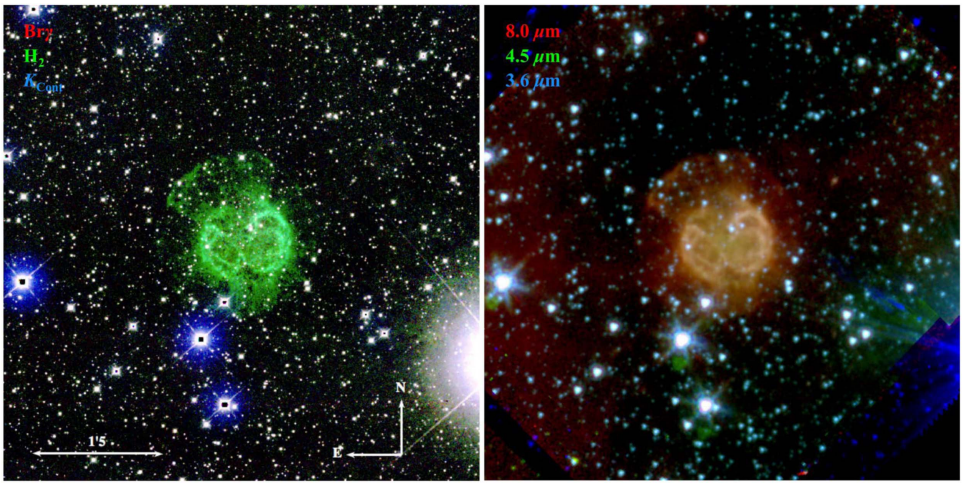

Figure 21. Left: CFHT color-composite image of NGC 7048. Right: *Spitzer* IRAC color-composite image of NGC 7048; image size and orientation are the same as on the left.

According to that definition scheme, Hb 12 and Sh 1-89 are bipolar PNe with equatorial waists, while NGC 6445 may belong to the broad-ring group. However, such a definition using apparent morphology alone could be insufficient to account for the intrinsic structures of all PNe. NGC 6720, NGC 6772, and NGC 6781 are nonbipolar in appearance but clearly ring-like; they have been suggested to be actually bipolar nebulae viewed at large inclination angles (Kastner et al. 1994). NGC 7048, although not so obvious as those three PNe, is suggestively ring-like (Kastner et al. 1996); in our CFHT H_2 image (Figures 2 and 22), the central region of this PN seems to resemble a disrupted ring. In the H_2 images of these four ring-like PNe, we detected halo features surrounding the bright central nebula/ring.

The halo of NGC 6720 has been observed from near- to far-IR (e.g., van Hoof et al. 2010). It is composed of an inner fragmented component and an outer circular one. The structure of NGC 6720 is highly disputed: either a closed, ellipsoidal nebular shell surrounded by the remnant red giant halo (Guerrero et al. 1997), or a bipolar PN with a nearly pole-on triple biconic structure (a counterpart of NGC 6853, Kwok et al. 2008), or a density-enhanced main ring with bipolar lobes

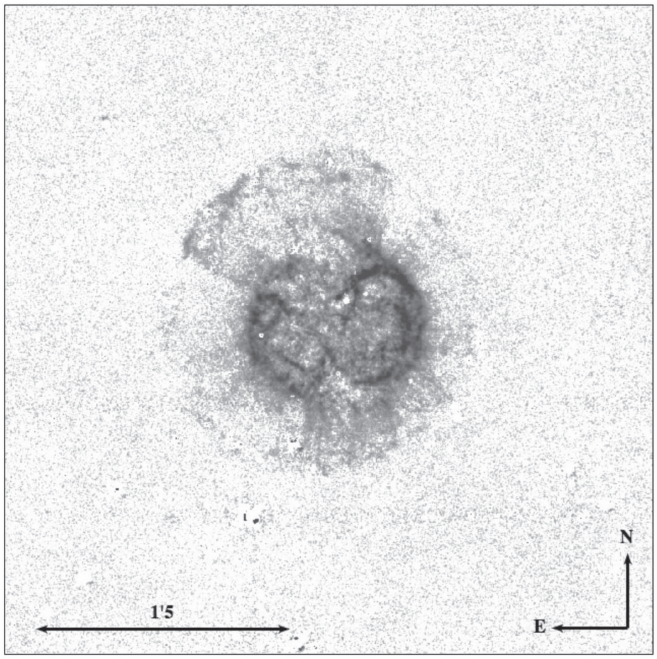

Figure 22. Residual image of NGC 7048 created by subtracting the scaled Brγ image from the H_2 image.

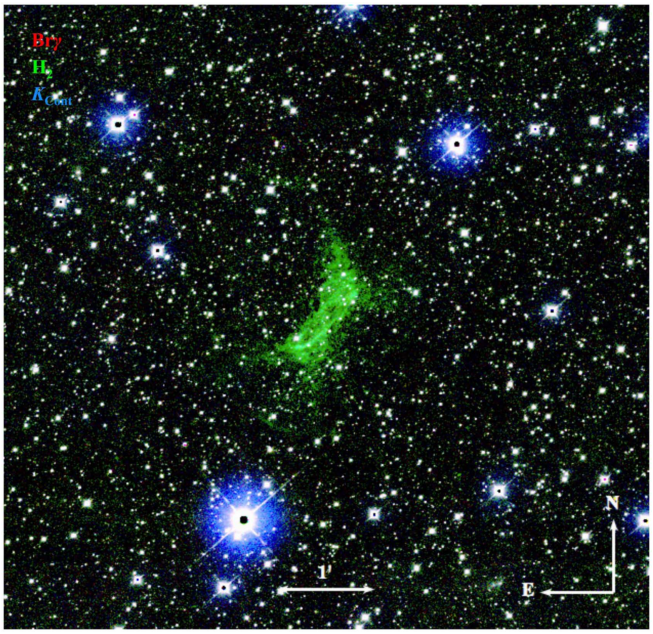

Figure 23. CFHT color-composite image of Sh 1-89. The central torus and bipolar morphology are visible in H_2 emission (green).

plus inner and outer halos (O'Dell et al. 2013). The detection of a faint crescent-shaped structure attached to the outer circular halo of NGC 6720 (Figure 11; similar to the case of the "Eskimo Nebula" NGC 2392, see Figure 1 of Zhang et al. 2012a) seems to be suggestive of a highly inclined bipolar nebula; however, careful investigation that combines the morphological and spatially resolved kinematic information is needed to discern the exact structure of this PN.

NGC 6781 was suggested to be a butterfly nebula, similar to NGC 2346, but oriented with its polar axis close to the line of sight (Balick 1987). It was observed in H_2 and identified as a low-surface-brightness counterpart to NGC 6720 (Zuckerman et al. 1990). Optical imagery of NGC 6781 reveals a $\sim$1′-radius bright ring with arcs and filaments extending along PA $\sim$ 160°. Morphokinematic observations of molecular lines (Zuckerman et al. 1990; Bachiller et al. 1993; Hiriart 2005) and photoionization modeling (Schwarz & Monteiro 2006) of this PN indicate that the central region of NGC 6781 probably resembles an open-ended cylindrical barrel oriented nearly pole-on; inside the barrel is a central cavity filled with fully ionized hot gas. Recent optical and mid-IR observations of NGC 6781 also suggested that it could be a bipolar PN oriented close to the line of sight (Phillips et al. 2011). Even more recent *Herschel* far-IR broadband imaging and spectroscopy confirmed the nearly pole-on barrel structure of NGC 6781 (Ueta et al. 2014).

Our deep H_2 imagery not only demonstrates the structure of NGC 6781 in greater detail than all previous IR observations, but also reveals extended nebular features. The central H_2-bright ring and the adjacent arc features may be morphologically explained by a highly inclined bipolar nebula projected on the sky. The filaments or knots in H_2 emission within the elliptical inner nebular shell may be patches of H_2 in the central ionized region (Otsuka et al. 2017). High spatial resolution optical images of NGC 6781 show knots as well as dark lanes across the region within the bright ring, indicating the existence of neutral filaments and condensations, which are probably associated with H_2 emission (Phillips et al. 2011).

The seven PNe discussed above, either bipolar or ring-like in the entirety of their morphologies, are mostly confined within 200 pc from the Galactic midplane (Table 1), which is consistent with the previous statistical studies (e.g., Kastner et al. 1996).

4.2. Origin of the Molecular Structure

The H_2 2.122 μm line emission has been used to trace not only the molecular component in PNe but also the interaction between stellar outflows and the circumstellar material. Detailed imaging studies with high spatial resolution suggest that the bright H_2 emission from the equatorial ring of bipolar PNe, instead of arising from the photodissociation regions shielded from the bright UV radiation by the ring, actually comes from dense knots or clumps embedded in the ionized gas (e.g., Cox et al. 1998; Speck et al. 2002, 2003; Matsuura et al. 2009; Marquez-Lugo et al. 2013; Manchado et al. 2015). Whether the H_2 in the knots within the nebular ring survived through the post-AGB evolution, or were destroyed and then formed again, was discussed by van Hoof et al. (2010) for the case of NGC 6720. Theoretical calculations have shown that H_2 may survive in the ionized region of PNe (Aleman & Gruenwald 2004) and that H_2 emission in the ionized nebulae can be important, particularly for the PNe with high-temperature central stars (Phillips 2006; Aleman & Gruenwald 2011). This qualitatively explains the higher detection rate of H_2 emission in bipolar PNe (i.e., Gatley's rule), given that these PNe usually have hotter central stars.

Several mechanisms have been proposed to explain the formation of these molecular knots in PNe, including the preexisting high-density structures in the ISM (Alūzas et al. 2012) and fragmentation of the swept-up nebular shell after termination of the fast stellar wind (García-Segura et al. 2006). In the latter paradigm, when the stellar wind declines or ceases, the hot, shocked bubble depressurizes and the thermal pressure of the photoionized region at the inner

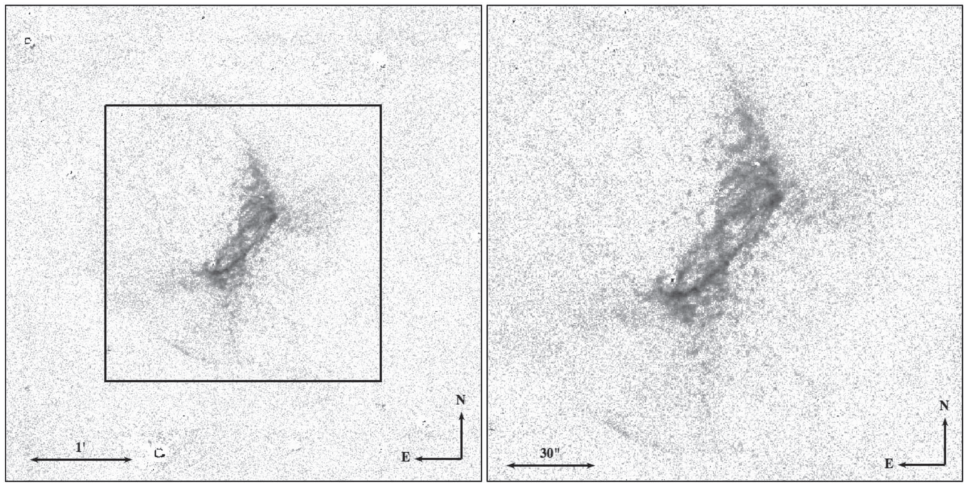

Figure 24. Left: residual image of Sh 1-89 created by subtracting the scaled Brγ image from the H_2 image. Right: zoom-in of the central region as marked by a black square in the left panel, showing details of the central ring structure.

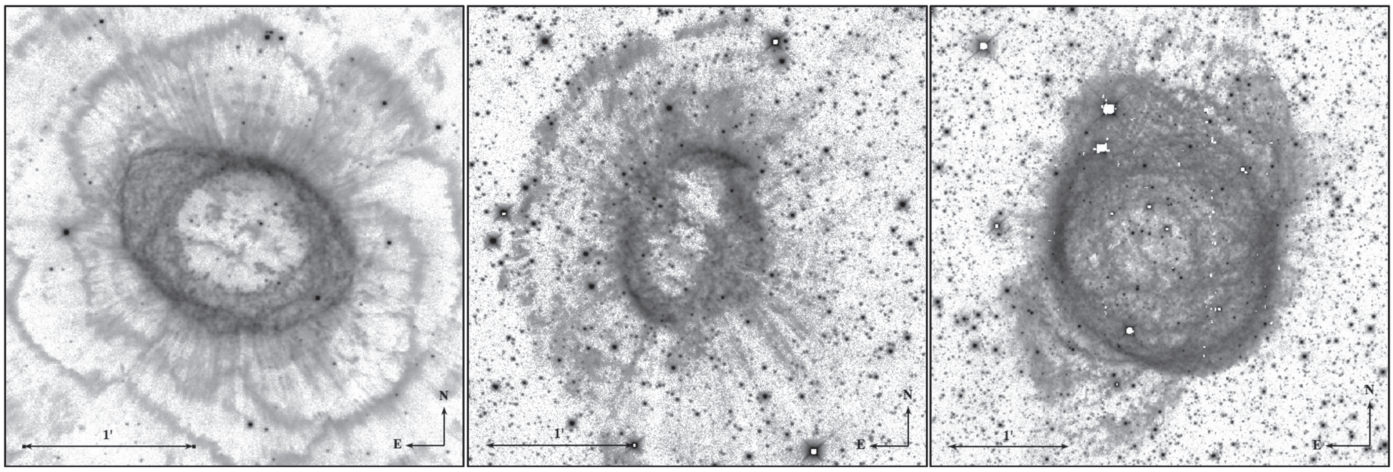

Figure 25. Close-up of the CFHT H_2 images of NGC 6720 (left), NGC 6772 (middle), and NGC 6781 (right) showing the fine-structure features of the central regions in detail.

edge of the swept-up shell becomes dominant; the nebular shell then fragments due to the Rayleigh–Taylor instability or the effects of ionizing radiation in the nebula, leading to the formation of neutral gas clumps with comet-like tails (García-Segura et al. 1999; see also hydrodynamical simulations by Toalá & Arthur 2014, 2016 for the formation of PNe).

As a benchmark case study of H_2 emission in PNe, the very high spatial resolution (≈60–90 mas) imaging of the bipolar PN NGC 2346 by Manchado et al. (2015) demonstrates well that H_2 emission in the equatorial ring comes from the fragmented clump region of NGC 2346 and appears to be uniform at lower resolutions. In our sample, Sh 1-89 is an archetypal counterpart to NGC 2346 in morphology. In the optical, Sh 1-89 has a bipolar structure (Figure 1), but the H_2 emission is mostly concentrated in the equatorial region. The residual H_2 image of Sh 1-89 clearly shows the fine clumpy features distributed along a tilted equatorial ring (Figure 24). This similarity between the two PNe in both the macro- and micromorphologies indicates that the formation mechanism of the H_2 in Sh 1-89 might be the same as in NGC 2346.

Similar clumpy fine-structure features of H_2 are also seen in NGC 6720, NGC 6772, and NGC 6781: numerous H_2-emitting knots or clumps are densely located within the central rings of the three ring-like PNe (Figure 25). In the H_2 images of both NGC 6720 and NGC 6772, we also observed radial filaments or rays coming out from the knots on the ring, which might be morphologically interpreted by the hydrodynamical simulations of García-Segura et al. (2006): when the effect of the fast stellar wind becomes negligible, the inner hot, shocked bubble depressurizes, and the swept-up nebular shell then fragments due to instability of the thermal pressure in the photoionized region; this process creates clumps with cometary tails and long, photoionized trails in between. The fast stellar wind from the central star probably does not account for the formation of these clumps. These radial rays are not quite obvious in the H_2 image of NGC 6781 but are visible in its residual H_2 image (see Figure 15). The fact that no X-ray emission was detected in these three PNe by *Chandra* (Kastner et al. 2012) also indicates that the stellar winds from their central stars had probably already declined.

At the distance to NGC 6781 (0.46–0.72 kpc, Frew et al. 2016; Otsuka et al. 2017), the pixel size 0.″3 of CFHT WIRCam corresponds to 138–216 au ($2.06–3.23 \times 10^{15}$ cm), which is comparable to the sizes of the H_2 clumps in NGC 2346 (112–238 au, Manchado et al. 2015). For the more distant PN Sh 1-89 (1.85 kpc), the pixel size of WIRCam

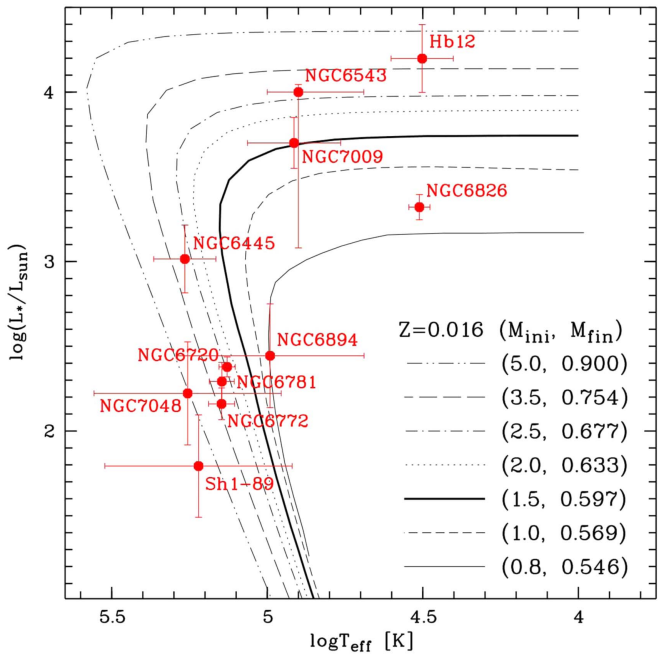

Figure 26. Locations of PN central stars in the H-R diagram along with errors in T_e and L_*. Different line types represent post-AGB evolutionary tracks of stars with different initial and final masses (M_{ini} and M_{fin}, in units of $M_\odot$; see the legend); model tracks are adopted from Vassiliadis & Wood (1994).

corresponds to 555 au (or 8.30×10^{15} cm). The distance to NGC 6772 (1.31 kpc) is between these two PNe. With higher spatial resolutions, we should expect to see the clumpy structures in the three PNe with much greater detail.

Excitation of H_2 emission and the nebular morphology are closely related to the evolutionary status of the PN central star. The locations of our targets in the Hertzsprung–Russell (H-R) diagram are shown in Figure 26, where the post-AGB evolutionary tracks calculated by Vassiliadis & Wood (1994) are presented. The effective temperatures and luminosities (as well as the uncertainties) of the PN central stars were adopted from the literature (Zhang & Kwok 1993; van Hoof et al. 2000, 2010; Stanghellini et al. 2002; Sabbadin et al. 2004; Wesson & Liu 2004; Walsh et al. 2016; Otsuka et al. 2017). According to their locations in the H-R diagram, the central stars of our sample might be separated into two main groups: those already on the cooling track (NGC 6720, NGC 6772, NGC 6781, NGC 6894, NGC 7048, Sh 1-89), and those whose temperatures are still increasing (Hb 12, NGC 6543, NGC 6826, NGC 7009). This general classification of the sample still stands if the most up-to-date post-AGB evolutionary tracks of Miller Bertolami (2016) are used.

Among the objects in the former group, NGC 6720 is so far the best studied in terms of morphology and origin of H_2. It is quite probable that in the post-AGB evolution, H_2 in the inner bright ring of NGC 6720 was first destroyed and then formed again later inside the knots after the central star entered the cooling track (see the discussion in van Hoof et al. 2010). However, if stellar evolution is fast enough, H_2 may still survive in the clumps. For the other PNe with central stars on the cooling track, H_2 in the equatorial ring might have formed through a similar mechanism. The exact formation and excitation mechanisms of H_2 emission in the halos of these PNe have never been studied, although it is common sense that H_2 in a PN halo was originally formed in the dense AGB wind and survived. The H_2 emission in the halos of these PNe could be shock excited, given that the radiation field of the central star could be too dilute at the distance of the halo. Alternatively, H_2 in the halo might have all been destroyed in the earlier post-AGB evolution of the central star, but formed later after the halo nebular gas recombined.

4.3. Possible Interaction with the ISM

Interaction of PNe and AGB winds (envelopes) with the ISM is an important process. It can be used as a tool to (1) study the evolution of PNe and their halos, (2) predict the proper motion of the central stars of PNe, and (3) probe the structure and physical properties of the ISM. The interaction is also key for solving the "missing-mass problem." This PN-ISM interaction usually affects the nebular morphology, especially the outer structures. Observational studies (e.g., Borkowski et al. 1990; Ramos-Larios & Phillips 2009; Sahai & Chronopoulos 2010; Ali et al. 2012, 2013; Zhang et al. 2012b; Sahai & Mack-Crane 2014; Ramos-Larios et al. 2018) and theoretical modeling (e.g., Dgani & Soker 1998; Villaver et al. 2003; Villaver 2004; Wareing et al. 2007a, 2007b) have been carried out to investigate such interactions. The consequences of interaction with the ISM are visually manifested as displacement of the central star from the geometric center of the nebula, or shifting of the nebular shell from the outer halo. The former case is usually seen in the optical bands, while the latter can be witnessed in the IR (e.g., Ramos-Larios & Phillips 2009). Ali et al. (2012) presented a catalog of 117 Galactic PNe that have interaction with the ISM, thus providing a unique database for such studies.

NGC 6772 is the best candidate in our sample that shows possible interaction with the ISM. An extended, asymmetric halo is seen in H_2 emission (Figure 12, left). The inner nebular shell, bright in the optical, is shifted toward the east. The eastern part of its halo seems to be compressed and limb-brightened, while the western halo is more extended in the form of a giant "loop." The eastern halo is brighter than the distorted western part in the mid-IR (Ramos-Larios & Phillips 2009). This difference in brightness is also seen in our H_2 image; moreover, we notice that the eastern halo shell is somewhat fragmented. This morphology indicates that NGC 6772 is probably interacting with the ISM.

We made a radial cut through the central star of NGC 6772 to check the emission profile of H_2, as shown in Figure 27, where the effect of enhanced shell-brightening due to interaction with the ISM is seen in the eastern halo (while the emission of the faint, much extended, diffuse western halo is marginally visible). The inner ring of NGC 6772 also seems to be distorted: emission of the west part seems to be more diffuse than the east, suggesting that interaction with the ISM not only shapes (and fragments) the outer halo of NGC 6772, but might also deform its inner region. Compared to H_2, Brγ emission in NGC 6772 is more homogeneous and only confined within the inner region (see Figure 2), so subtraction of the Brγ image from the H_2 image probably does not affect H_2 emission in the halo. Hence, the emission profile of H_2 in NGC 6772, at least for the outer halo (i.e., the east and west halos defined in Figure 13), is reliable.

An asymmetric halo seems to be surrounding the central nebula of NGC 7048, with H_2 emission enhancement generally along the NS direction (Figures 2 and 22). We anticipate there might be interaction between NGC 7048 and the ISM. The halo

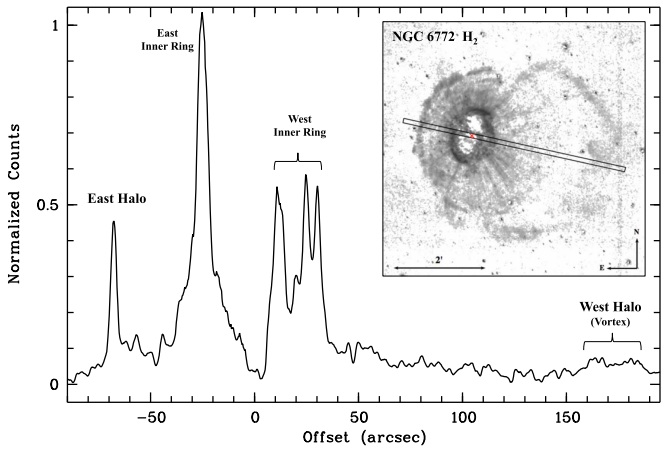

Figure 27. H_2 emission profile along a cut through the central star of NGC 6772 at PA = 77° (see the inset image; the cut width is 20 pixels, corresponding to 6″), in parallel with the possible proper motion direction (Figure 13, right). Both the image and emission profile have been slightly smoothed to reduce noise. Horizontal axis is the distance (in arcseconds) from the central star (red cross marked in the inset) defined to increase from east to west.

features in NGC 6781 are very faint in H_2 emission, compared to the other ring-like objects such as NGC 6720, NGC 6772, and NGC 7048 (see description in Section 3.6). However, the *Herschel* Planetary Nebula Survey (HerPlaNS) found a surrounding halo in NGC 6781 in far-IR emission (through the PACS/SPIRE broadband imaging; Ueta et al. 2014), indicating the existence of a cold dust component. No halo is seen in NGC 6894 in H_2, although this PN is ring-like. It has been proposed that the halo of NGC 6894 was stripped by the ISM (Soker & Zucker 1997).

We checked the surroundings of our targets to seek the possibility of PN-ISM interaction using the *WISE* archival images obtained from IRSA (see Section 2.5). The *WISE* images show that the four ring-like objects, NGC 6772, NGC 6781, NGC 6894, and NGC 7048, as well as two bipolar nebulae, Hb 12 and Sh1-89, might be located within huge volumes of the ISM that are seen in 12 μm emission (Figure 28); however, whether these ISM are truly associated (i.e., interacting) with these PNe, or simply the foreground/background material projected on the sky, needs to be confirmed. In our optical image, a giant [N II]-emitting filament intersects with the southwest lobe of Sh 1-89 (Figure 1), which might be indicative of interaction with the ISM. To confirm this, a follow-up study of Sh 1-89 through deep, wide-field optical imaging and high-dispersion spectroscopy will be underway (X. Fang et al. 2018, in preparation).

In the *WISE* image, we noticed a long feature close to NGC 6894 in 12 μm emission, stretching along the NE–SW direction (Figure 28, bottom left). This feature generally coincides in spatial distribution with the "stripes" seen in the Hα image (Soker & Zucker 1997, Figure 1 therein). Based on the orientation and morphologies seen in Hα, Soker & Zucker (1997) suggest that these "stripes" near (more specifically, to the northwest of) NGC 6894 may actually belong to the ionized halo of this PN that was stripped by the ISM. However, the detailed stripe-like structures as shown in the Hα image cannot be resolved in Figure 28 due to the low resolution (6.″1–6.″5) of the *WISE* image.

We also checked the *WISE* archive for the other five PNe (NGC 6445, NGC 6543, NGC 6720, NGC 6826, and NGC 7009) in our sample, and we found that either they are so bright in the *WISE* bands (especially in *W*3) that they outshine the nearby sky regions, or there is no surrounding ISM nearby. It is noteworthy that NGC 6772, NGC 6781, and NGC 6894 have already been identified as interacting PNe in Ali et al. (2012).[15]

As mentioned before, interaction with the ISM can strongly affect the outer structure of a PN (e.g., Wareing et al. 2007b). The nebula is compressed and limb-brightened in the direction of motion when a PN is moving through the ISM. In the residual H_2 image of NGC 6772 (Figure 13), a vortex structure is clearly seen at the westernmost part of its outer halo, extending to ∼3′ from the nebula center. This vortex, uncovered by the *Spitzer* image (Figure 12, right), is now discovered for the first time in this PN and has an angular extent of ∼2′, which corresponds to 0.75 pc (at a distance of 1.3 kpc, Stanghellini et al. 2008; Frew et al. 2016). This physical size of vortex is consistent with the hydrodynamical simulations of Wareing et al. (2007a), who predicted the size scale of vortices to be in the range 0.1–10 pc. A close inspection of Figure 13 also reveals that the AGB halo of NGC 6772 seems to have multiple layers: the western part of the outermost layer is in the process of disruption, while the eastern part is compressed, probably due to interaction with the ISM.

4.4. Mass-loss History: A Case Study of Hb 12

Extended structures of PNe are a result of a complex mass-loss process combined with stellar wind interaction (sometimes also interaction with the ISM). A careful morphological study of PNe with the aid of morphokinematic modeling can help us to better understand not only the wind interaction but also the mass-loss history of their immediate progenitors, the AGB stars. Here we briefly introduce a case study of Hb 12, which, compared to the other two bipolar PNe (NGC 6445 and Sh 1-89) in our sample, has much better defined bipolar lobes as well as microstructures. It is thus relatively easier to construct a morphological model for Hb 12.

The three coaxial, nested bipolar lobes observed in Hb 12 probably indicate that the collimated bipolar outflows (jets) were ejected at different episodes. This seems to be, to some extent, similar to the case of M 2-9, which probably has experienced multiple mass-loss events due to interaction of the binary stellar system at the center (Castro-Carrizo et al. 2012). Photometric observations suggest that the central star of Hb 12 could be a close binary system, which may be responsible for its bipolar morphology (Hsia et al. 2006). We thus speculate that the multiple coaxial bipolar lobes of Hb 12 reflect the mass-loss events that may also be related to the binary central star. However, very high resolution (such as the interferometric) observations are needed to resolve the physical structure and kinematics of the central equatorial region of Hb 12, which may in turn tell us the true nature of the central star.

The two pairs of knots along the direction of the polar axis signify interaction of the jets with the circumstellar material. In order to replicate the main features in Hb 12 as observed in our deep near-IR images (see the description in Section 3.1), we tried to construct a 3D morphological model using the software

[15] NGC 6826 was also considered as an interacting PN in Ali et al. (2012), but it is too bright in the *WISE* bands, and no obvious ambient ISM is seen nearby.

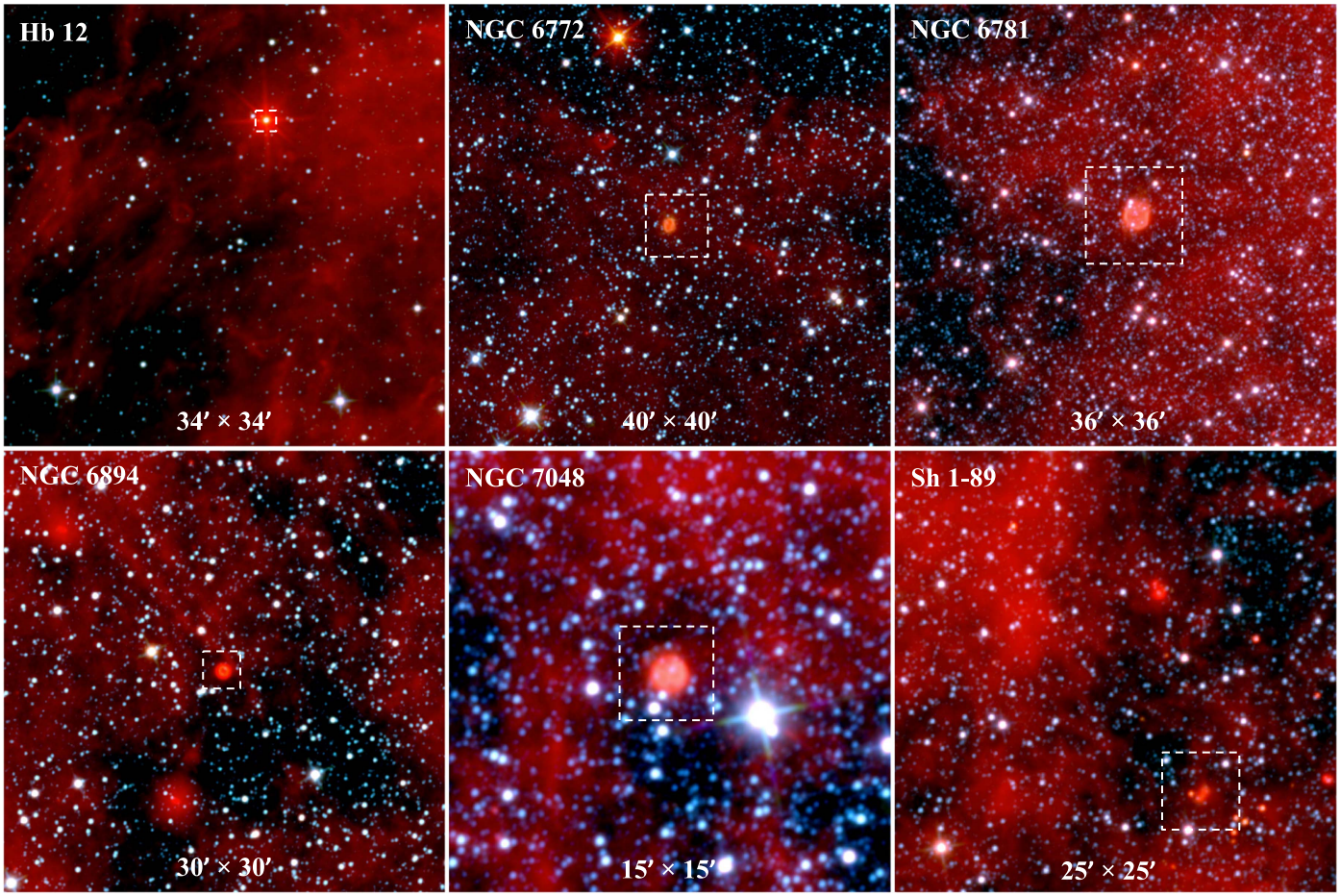

Figure 28. *WISE* color-composite pictures of Hb 12, NGC 6772, NGC 6781, NGC 6894, NGC 7048, and Sh 1-89 created with the *W*1 (3.4 μm, blue), *W*2 (4.6 μm, green), and *W*3 (12 μm, red) bands. Image size is indicated at the bottom of each panel; north is up and east to the left. In each panel, the white dashed square marks the field of view of the CFHT images of this PN in Figure 2.

SHAPE (Steffen & López 2006; Steffen et al. 2011). Figure 29 shows a comparison of the 3D model with the H_2+[N II] image of Hb 12 (see also Figure 4, left); a detailed description of the model will be presented in a subsequent paper (C.-H. Hsia et al. 2018, in preparation). Although velocity information is still needed to better model the 3D structures, at this stage we may conclude that it is possible to reproduce the central eye-shaped structure without an equatorial torus.

5. Summary and Conclusion

We report sensitive, near-IR observations of a sample of Galactic PNe using WIRCam on CFHT, aiming to search for extended nebular structures through deep imaging in the H_2 2.122 μm line emission. Thanks to the large FoV and high dynamic range of the detector, we observed highly intriguing nebular structures in a few objects. In several PNe of our sample, we detected extended structures in H_2 emission, and some of these structures were detected for the first time. These CFHT images were studied in contrast with the available optical images obtained from the *HST* archive and ground-based telescopes. The morphologies of our targets in H_2 were described in detail, and their significance in the shaping of PNe, stellar wind interaction, AGB mass loss, and the PN-ISM interaction is discussed.

A particular case is the bipolar nebula Hb 12. In the CFHT H_2 image of Hb 12, we observed (1) three coaxial, nested bipolar lobes, (2) a few arc features on either side of the central star probably due to inclined coaxial rings aligned along the outer bipolar lobes, and (3) two pairs of faint, point-symmetric knots about the central star distributed along the polar axis with slight misalignment. The outer pair of knots is the first detection in Hb 12. The overall morphology of Hb 12 resembles several other hourglass-shaped nebulae, including "Minkowski's Butterfly" M 2-9, which has a binary stellar system at the center and may have experienced multiple episodes of mass loss. We briefly introduced a morphological SHAPE model of this PN, which will be described in detail in a separate paper.

Structures of our sample PNe imaged in the H_2 line emission were discussed in the context of the long-established H_2 emission versus bipolarity relation (i.e., *Gatley's rule*). The ring-like objects in our sample might actually be the bipolar nebulae highly inclined with respect to the line of sight. However, this is merely a speculation for these ring-like nebulae based on the morphologies as seen in H_2; careful investigation utilizing kinematic information is needed. For several ring-like PNe that were previously suggested to be bipolar, our high spatial resolution imaging in H_2 resolves their central regions into numerous knotty or filamentary fine-structure features, which confirms the previous finding that H_2 emission mostly comes from the discrete knots or clumps embedded within the fully ionized gas at the equatorial regions of PNe.

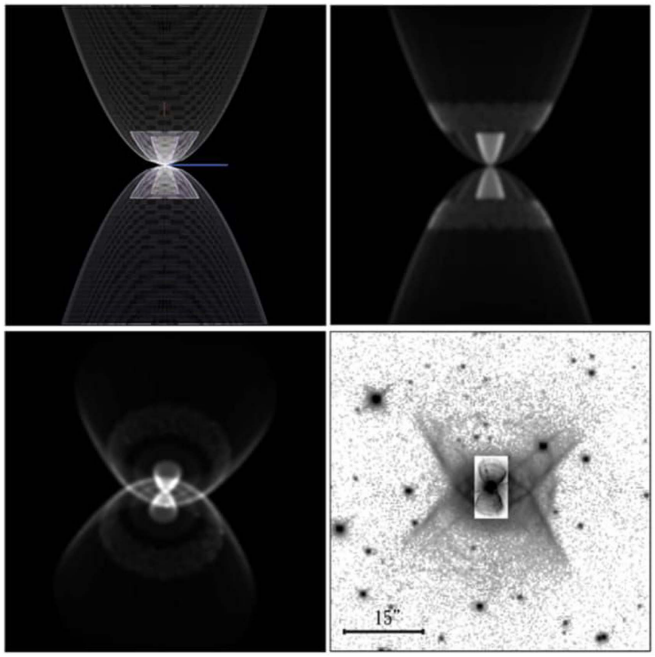

Figure 29. Comparison between the 3D SHAPE model (top and bottom-left panels) and the optical+IR image (bottom right) of Hb 12. The top left panel shows the model with an inclination angle of 0° (i.e., the polar axis lies in the plane of the sky), and the top right panel is the rendered image with the same inclination angle. The bottom left panel is the rendered image tilted with an inclination angle of ∼45° (and PA = 2°) to reproduce the equatorial "eye" structures seen in the optical+IR image presented in the bottom right panel, which is displayed by our CFHT WIRCam H_2 image and the inset *HST* Hα image at the center.

For the first time, the asymmetric halo of NGC 6772 was fully unveiled in H_2 emission, which probably is a result of interaction with the ISM. At the westernmost region of the highly distorted halo of NGC 6772, we spotted a "vortex," which could be due to the hydrodynamical effects. Several other objects in our CFHT sample have also been reported to be interacting PNe. We checked the *WISE* database and found that more than half of our sample, including the two bipolar nebulae Hb 12 and Sh 1-89, seem to be surrounded by huge volumes of the ISM visible in 12 μm. Whether these ISM are truly associated with the PNe or are simply the foreground/background projections is still unclear. It is worthwhile to investigate these PNe with respect to their surrounding environments. The southwest lobe of the butterfly-shaped Sh 1-89 is intersected by a giant filament that is bright in [N II], which might also be indicative of interaction with the ISM. Besides, in the residual H_2 image, the central equatorial region of Sh 1-89 clearly displays a tilted ring structure.

We observed a giant, patchy halo in H_2 surrounding the bright central region of NGC 6543; the overall morphology of these H_2 features generally follows the optical features in [S II] and [N II]. In NGC 7009, we found very faint, knotty/filamentary halo features in H_2 that are distributed as far as $\sim 2'$ from the central star. These halo H_2 features might be shock excited by the fast stellar wind that escaped from the central nebula; this possible mechanism seems to be consistent with the *Chandra* detection of extended X-ray emission within the inner hot bubbles of the two PNe.

This work well demonstrates the advantage of IR, wide-field sensitive imaging in studying the extended halo structures of PNe that are usually invisible in the optical bands. Given its extensive distribution, H_2 is an excellent tracer of both the ionized and molecular regions of a PN. Multiwavelength observations are essential to searching the full extent of PNe; moreover, kinematic measurements are needed to investigate the intrinsic structures of PNe. Despite our detailed description of the CFHT near-IR images, interpretation of some of the nebular structures presented in this work is still speculative, due to the lack of kinematic information. Follow-up morphokinematic studies of some of these PNe are highly desirable.

Part of the data presented here were obtained with ALFOSC, which is provided by the Instituto de Astrofísica de Andalucía (IAA-CSIC) under a joint agreement with the University of Copenhagen and NOSTA, and the 1.5 m telescope at San Pedro Mártir of the National Astronomical Observatory (OAN) operated by Universidad Nacional Autónoma de México (UNAM). Financial support for this work was provided by the Research Grants Council of Hong Kong under grant HKU 7027/11P C.-H.H. acknowledges financial support from the Science and Technology Development Fund of Macau (project No. 119/2017/A3 and 061/2017/A2). M.A.G. acknowledges support of the grant AYA 2014-57280-P, cofunded with FEDER funds. This research uses data obtained through the Telescope Access Program (TAP), which has been funded by the National Astronomical Observatories of China, the Chinese Academy of Sciences (the Strategic Priority Research Program "The Emergence of Cosmological Structures" Grant No. XDB09000000), and the Special Fund for Astronomy from the Ministry of Finance. This research made use of the SIMBAD database, operated at CDS, Strasbourg, France, and of NASA's Astrophysics Data System Bibliographic Services. We thank Quentin A. Parker and Foteini Lykou for their reading of the manuscript and comments. This research has made use of the *HST* archival data from MAST, the Mikulski Archive for Space Telescope at the Space Telescope Science Institute (STScI), which is operated by the Association of Universities for Research in Astronomy, Inc., under NASA contract NAS5-26555. Support for MAST for non-*HST* data is provided by the NASA Office of Space Science via grant NAG5-7584 and by other grants and contracts. This publication makes use of data products from the *Wide-field Infrared Survey Explorer* (*WISE*), which is a joint project of the University of California, Los Angeles, and the Jet Propulsion Laboratory/California Institute of Technology, funded by the National Aeronautics and Space Administration. This research also utilized the software SAOImage DS9 (Joye & Mandel 2003) developed by the Smithsonian Astrophysical Observatory.

Facilities: CFHT (WIRCam), NOT (ALFOSC), OAN-SPM:1.5 m.

ORCID iDs

Xuan Fang https://orcid.org/0000-0002-3981-7355
Sun Kwok https://orcid.org/0000-0001-7708-081X
Martín A. Guerrero https://orcid.org/0000-0002-7759-106X

References

Aaquist, O. B., & Kwok, S. 1990, A&AS, 84, 229
Akras, S., Gonçalves, D. R., & Ramos-Larios, G. 2017, MNRAS, 465, 1289
Aleman, I., & Gruenwald, R. 2004, ApJ, 607, 865
Aleman, I., & Gruenwald, R. 2011, A&A, 528, A74
Ali, A., Ismail, H. A., Snaid, S., & Sabin, L. 2013, A&A, 558, A93
Ali, A., Sabin, L., Snaid, S., & Basurah, H. M. 2012, A&A, 541, A98

Aller, L. H., Czyzak, S. J., Craine, E., & Kaler, J. B. 1973, ApJ, 182, 509
Alūzas, R., Pittard, J. M., Hartquist, T. W., Falle, S. A. E. G., & Langton, R. 2012, MNRAS, 425, 2212
Arias, L., Rosado, M., Salas, L., & Cruz-González, I. 2001, AJ, 122, 3293
Bachiller, R., Huggins, P. J., Cox, P., & Forveille, T. 1993, A&A, 267, 177
Balick, B. 1987, AJ, 94, 671
Balick, B. 2004, AJ, 127, 2262
Balick, B., & Frank, A. 2002, ARA&A, 40, 439
Balick, B., Gonzalez, G., Frank, A., & Jacoby, G. H. 1992, ApJ, 392, 582
Balick, B., & Hajian, A. R. 2004, AJ, 127, 2269
Balick, B., Wilson, J., & Hajian, A. R. 2001, AJ, 121, 354
Beckwith, S., Persson, S. E., & Gatley, I. 1978, ApJL, 219, L33
Black, J. H., & van Dishoeck, E. F. 1987, ApJ, 322, 412
Bohigas, J. 2003, RMxAA, 39, 149
Borkowski, K. J., Sarazin, C. L., & Soker, N. 1990, ApJ, 360, 173
Bryce, M., López, J. A., Holloway, A. J., & Meaburn, J. 1997, ApJL, 487, L161
Burton, M. G., Hollenbach, D. J., & Tielens, A. G. G. M. 1992, ApJ, 399, 563
Cahn, J. H., Kaler, J. B., & Stanghellini, L. 1992, A&AS, 94, 399
Castro-Carrizo, A., Bujarrabal, V., Neri, R., et al. 2017, A&A, 600, A4
Castro-Carrizo, A., Neri, R., Bujarrabal, V., et al. 2012, A&A, 545, A1
Chu, Y.-H., Jacoby, G. H., & Arendt, R. 1987, ApJS, 64, 529
Clark, D. M., López, J. A., Edwards, M. L., & Winge, C. 2014, AJ, 148, 98
Corradi, R. L. M., Livio, M., Balick, B., Munari, U., & Schwarz, H. E. 2001, ApJ, 553, 211
Corradi, R. L. M., Schönberner, D., Steffen, M., & Perinotto, M. 2003, MNRAS, 340, 417
Corradi, R. L. M., & Schwarz, H. E. 1995, A&A, 293, 871
Cox, P., Boulanger, F., Huggins, P. J., et al. 1998, ApJL, 495, L23
Davis, C. J., Smith, M. D., Stern, L., Kerr, T. H., & Chiar, J. E. 2003, MNRAS, 344, 262
Dgani, R., & Soker, N. 1998, ApJ, 495, 337
Dinerstein, H. L., Lester, D. F., Carr, J. S., & Harvey, P. M. 1988, ApJL, 327, L27
Dyson, J. E. 1992, MNRAS, 255, 460
Fazio, G. G., Hora, J. L., Allen, L. E., et al. 2004, ApJS, 154, 10
Forde, K. P., & Gledhill, T. M. 2012, MNRAS, 421, L49
Frew, D. J., Parker, Q. A., & Bojičić, I. S. 2016, MNRAS, 455, 1459
Froebrich, D., Davis, C. J., Joannidis, G., et al. 2011, MNRAS, 413, 480
Froebrich, D., Makin, S. V., Davis, C. J., et al. 2015, MNRAS, 454, 2586
García-Segura, G., Langer, N., Różyczka, M., & Franco, J. 1999, ApJ, 517, 767
García-Segura, G., López, J. A., Steffen, W., Meaburn, J., & Manchado, A. 2006, ApJL, 646, L61
Gledhill, T. M., & Froebrich, D. 2017, in IAU Symp. 323, Planetary Nebulae: Multi-wavelength Probes of Stellar and Galactic Evolution, ed. X.-W. Liu, L. Stanghellini, & A. I. Karakas (Cambridge: Cambridge Univ. Press), 32
Gonçalves, D. R., Corradi, R. L. M., Mampaso, A., & Perinotto, M. 2003, ApJ, 597, 975
Guerrero, M. A., Manchado, A., & Chu, Y.-H. 1997, ApJ, 487, 328
Guerrero, M. A., Villaver, E., Manchado, A., Garcia-Lario, P., & Prada, F. 2000, ApJS, 127, 125
Harrington, J. P., & Borkowski, K. J. 1994, BAAS, 26, 1469
Hiriart, D. 2005, A&A, 434, 181
Hora, J. L., & Latter, W. B. 1996, ApJ, 461, 288
Hora, J. L., Latter, W. B., & Deutsch, L. K. 1999, ApJS, 124, 195
Hrivnak, B. J., Smith, N., Su, K. Y. L., & Sahai, R. 2008, ApJ, 688, 327
Hsia, C.-H., Ip, W.-H., & Li, J.-Z. 2006, AJ, 131, 3040
Hsia, C.-H., Kwok, S., Chau, W., & Zhang, Y. 2016, JPhCS, 728, 2009
Hua, C.-T. 1997, A&AS, 125, 355
Huggins, P. J., Bachiller, R., Cox, P., & Forveille, T. 1996, A&A, 315, 284
Huggins, P. J., & Healy, A. P. 1986, MNRAS, 220, 33
Huggins, P. J., & Healy, A. P. 1989, ApJ, 346, 201
Hyung, S., & Aller, L. H. 1996, MNRAS, 278, 551
Isaacman, R. 1984, A&A, 130, 151
Joye, W. A., & Mandel, E. 2003, in ASP Conf. Ser. 295, Astronomical Data Analysis Software and Systems XII, ed. H. E. Payne, R. I. Jedrzejewski, & R. N. Hook (San Francisco, CA: ASP), 489
Kastner, J. H., Gatley, I., Merrill, K. M., Probst, R., & Weintraub, D. A. 1994, ApJ, 421, 600
Kastner, J. H., Montez, R., Jr, Balick, B., et al. 2012, AJ, 144, 58
Kastner, J. H., Weintraub, D. A., Gatley, I., Merrill, K. M., & Probst, R. 1996, ApJ, 462, 777
Kerber, F., Mignani, R. P., Guglielmetti, F., & Wicenec, A. 2003, A&A, 408, 1029
Kimura, R. K., Gruenwald, R., & Aleman, I. 2012, A&A, 541, A112
Kwok, S. 1982, ApJ, 258, 280
Kwok, S. 1983, in Proc. IAU Symp. 103, Planetary Nebulae, ed. D. R. Flower (Dordrecht: Reidel), 293
Kwok, S., Chong, S.-N., Koning, N., Hua, T., & Yan, C.-H. 2008, ApJ, 689, 219
Kwok, S., & Hsia, C.-H. 2007, ApJ, 805, 23
Kwok, S., Purton, C. R., & FitzGerald, M. P. 1978, ApJL, 219, L125
Latter, W. B., Kelly, D. M., Hora, J. L., & Deutsch, L. K. 1995, ApJS, 100, 159
López, J. A., Meaburn, J., Bryce, M., & Holloway, A. J. 1998, ApJ, 493, 803
Loup, C., Forveille, T., Omont, A., & Paul, J. F. 1993, A&AS, 99, 291
Manchado, A., Guerrero, M. A., Stanghellini, L., & Serra-Ricart, M. 1996, The IAC Morphological Catalog of Northern Galactic Planetary Nebulae (Tenerife: IAC)
Manchado, A., Stanghellini, L., Villaver, E., et al. 2015, ApJ, 808, 115
Marquez-Lugo, R. A., Guerrero, M. A., Ramos-Larios, G., & Miranda, L. F. 2015, MNRAS, 453, 1888
Marquez-Lugo, R. A., Ramos-Larios, G., Guerrero, M. A., & Vázquez, R. 2013, MNRAS, 429, 973
Matsuura, M., Speck, A. K., McHunu, B. M., et al. 2009, ApJ, 700, 1067
Meaburn, J., Walsh, J. R., Clegg, R. E. S., et al. 1992, MNRAS, 255, 177
Middlemass, D., Clegg, R. E. S., & Walsh, J. R. 1989, MNRAS, 239, 1
Middlemass, D., Clegg, R. E. S., Walsh, J. R., & Harrington, J. P. 1991, MNRAS, 251, 284
Miller Bertolami, M. M. 2016, A&A, 588, A25
Millikan, A. G. 1974, AJ, 79, 1259
Miranda, L. F., & Solf, J. 1989, A&A, 214, 353
Moreno-Corral, M. A., Fuente, E., & Gutiérrez, F. 1998, RMxAA, 34, 117
O'Dell, C. R., Ferland, G. J., Henney, W. J., & Peimbert, M. 2013, AJ, 145, 92
Otsuka, M., Ueta, T., van Hoof, P. A. M., et al. 2017, ApJS, 231, 22
Panagia, N., Scuderi, S., Gilmozzi, R., et al. 1996, ApJL, 459, L17
Peimbert, M., & Torres-Peimbert, S. 1983, in IAU Symp. 103, Planetary Nebulae, ed. D. R. Flower (Dordrecht: Reidel), 233
Perinotto, M. 1991, ApJS, 76, 687
Phillips, J. P. 2006, MNRAS, 368, 819
Phillips, J. P., & Ramos-Larios, G. 2010, MNRAS, 405, 2179
Phillips, J. P., Ramos-Larios, G., & Guerrero, M. A. 2011, MNRAS, 415, 513
Puget, P., Stadler, E., Doyon, R., et al. 2004, Proc. SPIE, 5492, 978
Ramos-Larios, G., Guerrero, M. A., & Miranda, L. F. 2008, AJ, 135, 1441
Ramos-Larios, G., Guerrero, M. A., Nigoche-Netro, A., et al. 2018, MNRAS, 475, 932
Ramos-Larios, G., Guerrero, M. A., Sabin, L., & Santamaría, E. 2017, MNRAS, 470, 3707
Ramos-Larios, G., Guerrero, M. A., Suárez, O., Miranda, L. F., & Gómez, J. F. 2012, A&A, 545, A20
Ramos-Larios, G., & Phillips, J. P. 2009, MNRAS, 400, 575
Ramsay, S. K., Chrysostomou, A., Geballe, T. R., Brand, P. W. J. L., & Mountain, M. 1993, MNRAS, 263, 695
Reed, D. S., Balick, B., Hajian, A., et al. 1999, AJ, 118, 2430
Sabbadin, F., Turatto, M., Cappellaro, E., Benetti, S., & Ragazzoni, R. 2004, A&A, 416, 955
Sahai, R., & Chronopoulos, C. K. 2010, ApJL, 711, L53
Sahai, R., Dayal, A., Watson, A. M., et al. 1999, AJ, 118, 468
Sahai, R., Hines, D. C., Kastner, J. H., et al. 1998, ApJL, 492, L163
Sahai, R., & Mack-Crane, G. P. 2014, ApJ, 148, 74
Sahai, R., Morris, M. R., & Villar, G. G. 2011, AJ, 141, 134
Sahai, R., & Trauger, J. T. 1998, AJ, 116, 1357
Schild, H. 1995, A&A, 297, 246
Schwarz, H. E., & Monteiro, H. 2006, ApJ, 648, 430
Shull, J. M., & Beckwith, S. 1982, ARA&A, 20, 163
Shupe, D. L., Armus, L., Matthews, K., & Soifer, B. T. 1995, AJ, 109, 1173
Soker, N., & Zucker, D. B. 1997, MNRAS, 289, 665
Speck, A. K., Meixner, M., Fong, D., et al. 2002, AJ, 123, 346
Speck, A. K., Meixner, M., Jacoby, G. H., & Knezek, P. M. 2003, PASP, 115, 170
Stanghellini, L., Shaw, R. A., & Villaver, E. 2008, ApJ, 689, 194
Stanghellini, L., Villaver, E., Manchado, A., & Guerrero, M. A. 2002, ApJ, 576, 285
Steffen, W., Koning, N., Wenger, S., Morisset, C., & Magnor, M. 2011, IEEE Trans. Vis. Comput. Graphics, 17, 454
Steffen, W., & López, J. A. 2006, RMxAA, 42, 99
Storey, J. W. V. 1984, MNRAS, 206, 521
Storey, J. W. V., Webster, B. L., Payne, P., & Dopita, M. A. 1987, in IAU Symp. 120, Astrochemistry, ed. M. S. Vardya & S. P. Tarafdar (Dordrecht: Reidel), 339
Sugerman, B. E. K., Crotts, A. P. S., Kunkel, W. E., Heathcote, S. R., & Lawrence, S. S. 2005, ApJS, 159, 60

Toalá, J. A., & Arthur, S. J. 2014, MNRAS, 443, 3486
Toalá, J. A., & Arthur, S. J. 2016, MNRAS, 463, 4438
Ueta, T., Ladjal, D., Exter, K. M., et al. 2014, A&A, 565, A36
van Hoof, P. A. M., Van de Steen, G. C., Beintema, D. A., et al. 2000, ApJ, 532, 384
van Hoof, P. A. M., Van de Steene, G. C., Barlow, M. J., et al. 2010, A&A, 518, L137
Vassiliadis, E., & Wood, P. R. 1994, ApJS, 92, 125
Vaytet, N. M. H., Rushton, A. P., Lloyd, M., et al. 2009, MNRAS, 398, 385
Vázquez, R., Zavala, S., Blanco, M. W., et al. 2004, BAAS, 205, 1571
Villaver, E. 2004, in ASP Conf. Ser. 313, Asymmetrical Planetary Nebulae III: Winds, Structure, and the Thunderbird, ed. M. Meixner et al. (San Francisco, CA: ASP), 426
Villaver, E., García-Segura, G., & Manchado, A. 2003, ApJL, 585, L49
Walsh, J. R., Monreal-Ibero, A., Barlow, M. J., et al. 2016, A&A, 588, A106
Wareing, C. J., Zijlstra, A. A., & O'Brien, T. J. 2007a, ApJL, 660, L129
Wareing, C. J., Zijlstra, A. A., & O'Brien, T. J. 2007b, MNRAS, 382, 1233
Webster, B. L., Payne, P. W., Storey, J. W. V., & Dopita, M. A. 1988, MNRAS, 235, 533
Wesson, R., & Liu, X.-W. 2004, MNRAS, 351, 1026
Wright, E. L., Eisenhardt, P. R. M., Mainzer, A. K., et al. 2010, AJ, 140, 1868
Zhang, C.-Y., & Kwok, S. 1990, A&A, 237, 479
Zhang, C.-Y., & Kwok, S. 1993, ApJS, 88, 137
Zhang, Y., Fang, X., Chau, W., et al. 2012a, ApJ, 754, 28
Zhang, Y., Hsia, C.-H., & Kwok, S. 2012b, ApJ, 755, 53
Zhang, Y., Kwok, S., & Ko, C.-M. 2012c, in Proc. IAU Symp. 283, Planetary Nebulae, ed. A. Manchado et al. (Cambridge: Cambridge Univ. Press), 530
Zuckerman, B., & Gatley, I. 1988, ApJ, 324, 501
Zuckerman, B., Kastner, J. H., Balick, B., & Gatley, I. 1990, ApJL, 356, L59